

Utrecht University Repository

Title	Higher-order symmetry plane correlations in Pb-Pb collisions at $\sqrt{s_{NN}}=5.02\text{TeV}$
Authors	ALICE Collaboration; Koster, Noor
Published in	Physical Review C
Publication Date	2025-06-30
Link	https://dspace.library.uu.nl/handle/1874/480597
Citation	ALICE Collaboration & Koster, N 2025, 'Higher-order symmetry plane correlations in Pb-Pb collisions at $\sqrt{s_{NN}}=5.02\text{TeV}$ ', Physical Review C, vol. 111, no. 6. https://doi.org/10.1103/zh6t-29hf
Versions / License	Publisher version
Rights	https://www.uu.nl/en/university-library/license-and-reuse-conditions

Higher-order symmetry plane correlations in Pb-Pb collisions at $\sqrt{s_{NN}} = 5.02$ TeVS. Acharya *et al.**
(ALICE Collaboration)

(Received 30 September 2024; accepted 30 May 2025; published 30 June 2025)

The correlations between event-by-event fluctuations of symmetry planes are measured in Pb-Pb collisions at a center-of-mass energy per nucleon pair $\sqrt{s_{NN}} = 5.02$ TeV recorded by the ALICE detector at the Large Hadron Collider. This analysis is conducted using the Gaussian estimator technique, which is insensitive to biases from correlations between different flow amplitudes. The study presents, for the first time, the centrality dependence of correlations involving up to five different symmetry planes. The correlation strength varies depending on the harmonic order of the symmetry plane and the collision centrality. Comparisons with measurements from lower energies indicate no significant differences within uncertainties. Additionally, the results are compared with hydrodynamic model calculations. Although the model predictions provide a qualitative explanation of the experimental results, they overestimate the data for some observables. This is particularly true for correlators that are sensitive to the nonlinear response of the medium to initial-state anisotropies in the collision system. As these new correlators provide unique information— independent of flow amplitudes—their usage in future model developments can further constrain the properties of the strongly interacting matter created in ultrarelativistic heavy-ion collisions.

DOI: [10.1103/zx6t-29hf](https://doi.org/10.1103/zx6t-29hf)**I. INTRODUCTION**

One of the most extensively studied phenomena in ultrarelativistic heavy-ion collisions is the collective behavior of the produced particles [1,2]. The nature of the created system and the interactions among particles involved make collectivity sensitive to all stages of the collision [3–10]. Moreover, previous studies, including Bayesian parameter estimations, have shown that the measurements of the correlations between the charged final-state particles are, in particular, a highly sensitive probe of the transport properties of the quark-gluon plasma (QGP) [6,9–14]. This extreme state of matter, created during the collision, consists of deconfined quarks and gluons, and exhibits quasiperfect liquidlike behavior. As the QGP cannot be directly observed and the evolving system is highly complex, it is crucial to develop and measure observables related to the collectivity of the final-state particles, which reflects the properties of the underlying medium. More details about the QGP studies can be found in Refs. [5–7,10,15,16].

One observable manifestation of the collective behavior of the detected particles is their anisotropic azimuthal emission in the transverse plane, known as the anisotropic flow. This phenomenon arises from the medium response to the non-isotropic initial-state geometry of the collision and the initial

inhomogeneities in the system's entropy density [1,17]. The azimuthal distribution of the final-state particles $f(\varphi)$ can be represented using a Fourier series as [17]

$$f(\varphi) = \frac{1}{2\pi} \left[1 + 2 \sum_n v_n \cos[n(\varphi - \Psi_n)] \right], \quad (1)$$

where v_n and Ψ_n denote the flow amplitudes and symmetry plane angles of the n th harmonic, respectively. The measurements and theoretical calculations of these quantities and their complex correlations play an important role in understanding the properties of QGP [12,13,18–22].

Flow amplitudes and symmetry planes, as well as their event-by-event fluctuations, are not directly accessible experimentally. Therefore, various approaches were developed to estimate them, such as the event plane method [23,24] or the multiparticle correlation techniques [25–29]. The latter, which are the focus of this analysis, rely on the relation between the measured particle azimuthal angles φ and the flow degrees of freedom v_n and Ψ_n [28–30]:

$$v_{n_1}^{a_1} \dots v_{n_k}^{a_k} e^{i(a_1 n_1 \Psi_{n_1} + \dots + a_k n_k \Psi_{n_k})} = \langle e^{i(n_1 \varphi_1 + \dots + n_l \varphi_l)} \rangle, \quad (2)$$

where $\langle \dots \rangle$ indicates an average over the azimuthal angles of distinct combinations of l particles in the same event. Given that the multiparticle azimuthal correlator contains k ($k \leq l$) different harmonics (counting positive and negative harmonics separately), the positive integers a_i are used to ensure each harmonic n_i appears only once on the left-hand side of Eq. (2). The order of the multiparticle azimuthal correlator l , which corresponds to the number of particles involved, is given by $l = \sum_i a_i$. Further details on the coefficients a_i and their interpretation can be found in Ref. [21].

*Full author list given at the end of the article.

In the last few years, significant progress has been made in the study of the flow amplitudes v_n . The flow coefficients themselves were measured for the harmonics from $n = 2$ [15,16,31–35] to $n = 9$ [18]. The first experimental studies of the symmetric cumulants (SC) by the ALICE Collaboration [12,13] showed the existence of non-negligible correlations between two different flow amplitudes v_m^2 and v_n^2 . This research was extended to include more flow amplitudes [19,20,36,37] and different moments of these amplitudes' distributions [20,22,37,38]. Comparisons between experimental results and theoretical calculations have demonstrated that the measurements of the SC are more sensitive to the transport properties of the QGP than the individual flow amplitudes [12]. Such a conclusion was recently confirmed with sensitivity studies conducted in Bayesian analyses [8,9]. These studies proved that flow observables involving higher-order harmonics or cumulants impose more constraints on the initial-state and hydrodynamic model parameters.

Similarly to the flow amplitudes, symmetry planes carry information about both the initial state of the collision and the QGP phase. As such, analyzing symmetry planes and their correlations provides additional insights into the QGP produced in those collisions. However, even in the case of collisions with impact parameters of the same magnitude in the absence of event-by-event fluctuations of the position of participating nucleons, the angle of each symmetry plane Ψ_n measured in the laboratory frame varies from one collision to another due to a different orientation of the impact parameter. This orientation is generally characterized as the angle of the reaction plane (Ψ_{RP}), which is a plane spanned by the impact parameter and the beam axis. The reaction plane angle Ψ_{RP} , therefore, changes from one event to another like $\Psi_{RP} \rightarrow \Psi_{RP} + \alpha$, where α is a random fluctuation. Hence, each individual symmetry plane shifts by $\Psi_n \rightarrow \Psi_n + \alpha$ in the laboratory frame from one collision to another. As a result, the averaged value of an individual symmetry plane measured in the laboratory is zero. Therefore, the simplest nontrivial observables are the correlated fluctuations of different symmetry planes with respect to each other, as the contribution of the reaction plane fluctuations cancels out. These are quantified by observables such as $\langle \cos[4(\Psi_4 - \Psi_2)] \rangle$, which is one example involving the symmetry planes Ψ_4 and Ψ_2 . The analysis of these symmetry plane correlations (SPC) presents unique challenges. For instance, any expression of SPC has to be rotationally invariant, ensuring that the random event-by-event fluctuations of the impact parameter vector do not affect the measurement. This can be achieved by a suitable choice of the harmonics n_i and coefficients a_i in Eq. (2) with the constraint $\sum a_i n_i = 0$. More details on the proper choice of these quantities, which lead to nontrivial SPC, can be found in Appendix B of Ref. [30].

When applying Eq. (2) in experimental measurements, it is not possible to find a set of harmonics such that the left-hand side of Eq. (2) only involves symmetry planes without the inclusion of flow amplitudes. As a solution to this, estimators of SPC were developed to remove the contribution of the flow amplitudes when using multiparticle correlation techniques. One of the most widely used methods to estimate the SPC is the so-called scalar product (SP) method [39,40], which was

used in the analyses of SPC in heavy-ion collisions at the Large Hadron Collider (LHC) energies by ATLAS [39] and ALICE [18,40]. The SP method is defined as

$$\begin{aligned} & \langle \cos(a_1 n_1 \Psi_{n_1} + \dots + a_k n_k \Psi_{n_k}) \rangle_{\text{SP}} \\ &= \frac{\langle v_{n_1}^{a_1} \dots v_{n_k}^{a_k} \cos(a_1 n_1 \Psi_{n_1} + \dots + a_k n_k \Psi_{n_k}) \rangle}{\sqrt{\langle v_{n_1}^{2a_1} \rangle \dots \langle v_{n_k}^{2a_k} \rangle}}, \end{aligned} \quad (3)$$

where both numerator and denominator can be estimated with multiparticle correlation techniques using Eq. (2). In this approach, one divides the numerator, which contains the mean of the product of flow amplitudes, by the product of their respective means in the denominator. Such a ratio, however, introduces a bias in the estimation of SPC as correlations among flow amplitudes imply that $\langle v_{n_1}^{a_1} \dots v_{n_k}^{a_k} \rangle \neq \langle v_{n_1}^{a_1} \rangle \dots \langle v_{n_k}^{a_k} \rangle$. This issue was resolved in the recent work of Ref. [30], which proposed a new estimator called the Gaussian estimator (GE). In the derivation of the GE, a two-dimensional Gaussian distribution was used to approximate multiharmonic flow fluctuations. This leads to the following expression for the estimation of SPC:

$$\begin{aligned} & \langle \cos(a_1 n_1 \Psi_{n_1} + \dots + a_k n_k \Psi_{n_k}) \rangle_{\text{GE}} \\ &= \sqrt{\frac{\pi}{4}} \frac{\langle v_{n_1}^{a_1} \dots v_{n_k}^{a_k} \cos(a_1 n_1 \Psi_{n_1} + \dots + a_k n_k \Psi_{n_k}) \rangle}{\sqrt{\langle v_{n_1}^{2a_1} \rangle \dots \langle v_{n_k}^{2a_k} \rangle}}. \end{aligned} \quad (4)$$

Again, both the numerator and denominator on the right-hand side of Eq. (4) can be estimated using Eq. (2). In contrast to the SP method [Eq. (3)], the denominator of the GE in Eq. (4) contains only the multivariate joint moment of the flow amplitudes $\langle v_{n_1}^{2a_1} \dots v_{n_k}^{2a_k} \rangle$. As such, the GE accounts for the correlations among the flow amplitudes, which overcomes the bias present in the SP method as demonstrated in Ref. [30]. Recently, the GE was used by ALICE in the study of SPC in Pb-Pb collisions at a center-of-mass energy per nucleon pair $\sqrt{s_{NN}} = 2.76$ TeV [21]. The correlations estimated with the GE were significantly smaller compared to the results obtained with the SP method by ATLAS [39] and ALICE [40]. This observation is qualitatively in agreement with the results in Ref. [30] and was attributed to the minimisation of the bias from neglecting the correlations among flow amplitudes. The removal of the bias is important in order to extract independent information about symmetry planes.

In this article, the GE is utilized in Pb-Pb collisions at $\sqrt{s_{NN}} = 5.02$ TeV. The large data set allows more SPC combinations to be studied including, for the first time, measurements involving up to five different symmetry planes. These provide a detailed study of how symmetry planes of different harmonics interplay, which is crucial for the understanding of the impact of linear and nonlinear hydrodynamic responses of the medium, whose evolution is governed by the strong force as described by the quantum chromodynamics (QCD). Additionally, by comparing results with those from Ref. [21], the energy dependence of SPC is explored.

The article is structured as follows. Section II presents the ALICE detector, the event and track selections of the analyzed data set, and the estimation of the statistical and systematic uncertainties. The results and their comparisons

with state-of-the-art theoretical predictions are discussed in Sec. III. Section IV provides a summary of the article. Additional results are shown in Appendixes A–C.

II. DATA ANALYSIS

This analysis is conducted using the Pb-Pb collision data sets at $\sqrt{s_{NN}} = 5.02$ TeV recorded by ALICE in 2015 and 2018. The detailed descriptions of the various detectors and their performance are given in Refs. [41,42].

For the triggering, event selection, and centrality determination, the V0 detector is used. This detector consists of two scintillator arrays, V0A and V0C [41,43]. The arrays cover the full azimuth and extend in pseudorapidity (η) over the ranges $2.8 < \eta < 5.1$ (V0A) and $-3.7 < \eta < -1.7$ (V0C). The centrality is determined from the V0 signal and is generally presented as a percentile of the total hadronic Pb-Pb cross section. The most central (head-on) collisions, which produce the largest number of particles, correspond to 0% percentile, while the more peripheral collisions are denoted with higher percentiles. Charged particle tracks are reconstructed using the Time Projection Chamber (TPC) [44], which covers the full azimuthal angle and $|\eta| < 0.9$ in the longitudinal direction. In addition to the TPC, the Inner Tracking System (ITS) [45,46] is used for track reconstruction. The ITS consists of six silicon layers, where the two innermost layers constitute the Silicon Pixel Detector (SPD). The SPD provides high-resolution space points for the determination of the track parameters in the vicinity of the beam axis and for the primary and secondary vertex reconstruction. Both the ITS and TPC, are placed in a homogeneous solenoidal magnetic field of 0.5 T in beam direction, whose polarity was reversed during the data taking.

For both 2015 and 2018 data sets, events are selected with the minimum bias (MB) trigger, which requires a coincident trigger signal from both V0A and V0C. Additional triggers for central and semicentral collisions are used for 2018 data to include more events in the centrality percentiles 0–10% and 30–50%, respectively. Furthermore, for the data taken in 2018, centrality flattening is applied by rejecting events to ensure a uniform distribution per centrality interval. With the uniform distribution, the centrality interval becomes properly averaged. Overall seven centrality classes within the range of 0–60% have been used for the analysis.

For the analysis, triggered events with a reconstructed primary vertex within ± 8.0 cm from the nominal interaction point along the beam line are selected to ensure a full geometrical acceptance of the ITS for $|\eta| < 0.9$. Background events such as beam-gas collisions and pileup were removed using the timing information from the V0 detector, the correlation between the primary vertex positions reconstructed from SPD tracklets and ITS+TPC tracks, and the correlation between the number of hits in the TPC and in the outer layers of the ITS [47]. A further rejection of particles produced in out-of-bunch pileup collisions was achieved by selecting tracks that either have a hit in the SPD, which has short readout time of 300 ns, or have a production time, measured with the time-of-flight detector [48], compatible with the bunch crossing that fired the trigger. Furthermore, this analysis requires

correlators involving up to 14 particles; therefore, a minimum of 14 reconstructed tracks per event was necessary to capture all needed particle correlations. Following these event selection criteria, the number of events used in the analysis is approximately 210 million.

The pseudorapidity and transverse momentum of the tracks are required to be in the intervals $|\eta| < 0.8$ and $0.2 < p_T < 5.0$ GeV/c. The lower p_T limit is set to remove tracks with low reconstruction efficiency, while the upper limit is set to reduce contamination from jets, which generally dominate at higher p_T . For each track, the distance of closest approach (DCA) to the primary vertex is required to be less than 2 cm along the longitudinal direction and less than $0.0105 + 0.0350/p_T^{1.1}$ cm in the transverse plane, where the p_T is in GeV/c. Thus, in the transverse direction, the DCA ranges from 0.016 cm ($p_T = 5.0$ GeV/c) to 0.22 cm ($p_T = 0.2$ GeV/c). The DCA value requirements on the tracks are used to reduce contamination from secondary particles originating from weak decays and interactions with the detector material. The contamination is largest for particles with low p_T , and it ranges from 20% (10%) for $p_T < 0.1$ GeV/c to less than 2% (1%) for $p_T > 1.0$ GeV/c in central (peripheral) collisions [49]. The contributions of correlations that do not arise from anisotropic flow were tested with HIJING simulations. The check was conducted separately for the numerator and denominator for all SPC. The resulting correlators from HIJING were compatible with zero, and thus had no contributions from nonflow. Furthermore, only tracks with a minimum of 70 out of 159 TPC space points are selected to guarantee precise tracking. The χ^2 per space point value is required to be between 0.1 and 2.5 to ensure a good fit of the tracks. In addition, a minimum of 2 hits in the ITS is required for each track. These selection criteria are consistent with those in Refs. [22,50].

The reconstructed tracks are corrected for their non-uniform reconstruction efficiency (NUE) as a function of p_T and for nonuniform azimuthal acceptance (NUA). The NUE corrections are obtained by constructing p_T -dependent weights for the tracks from simulations performed with HIJING (Heavy-Ion Jet INteraction Generator) [51] event generator in combination with GEANT 3 [52] transport code including a detailed description of the ALICE detectors and their efficiency. The NUE corrections are used to account for the reconstruction efficiency as a function of p_T and the contamination from secondary particles [49]. The applied NUA correction is data driven such that the data are first scanned to obtain weights to each cell in longitudinal (η) and azimuthal (φ) directions for each value of the longitudinal position of the primary vertex. The weights are then applied for each particle in the analysis.

Statistical uncertainties were determined by measuring variances of the numerator and denominator in Eq. (4) separately and then evaluating the full uncertainty with standard propagation of uncertainty. The procedure is identical to the one used in Ref. [21] for the analysis of Pb-Pb collisions at $\sqrt{s_{NN}} = 2.76$ TeV.

To evaluate the systematic uncertainties, the selection criteria are varied one by one and the results are compared with those obtained with the nominal selections. The recommendations from Ref. [53] are used to determine the significance

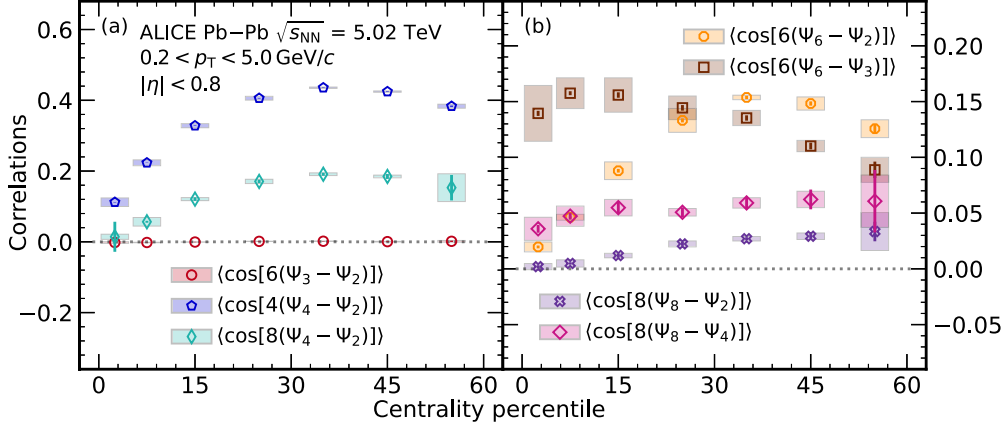


FIG. 1. Magnitude of SPC between two symmetry planes. The statistical and systematic uncertainties are depicted as lines and boxes, respectively.

of separate systematic trials. This test for statistical significance is sometimes called *the Barlow test*. If for a trial the difference to the default value divided by the uncertainty of that difference is greater than 1, then the relative variation of the results obtained with this modified selection is considered to be significant within statistical uncertainties. The trial is then included as a systematic uncertainty. Finally, the total systematic uncertainty is calculated for each centrality class by summing the significant sources in quadrature.

In the following, the different specific contributions to the systematic uncertainty are presented and for each of them the average value of the uncertainty (averaged over centrality classes and SPC observables) is reported in parentheses. The impact of the variable used to determine the centrality is estimated by substituting the default centrality estimator from energy deposition in the V0 scintillator with an estimate based on the number of hits in the first layers of the ITS (12%). In the event selection, systematic uncertainties are estimated by varying the selection on the longitudinal position of the primary vertex from ± 8 to ± 7 and ± 9 cm (9%), and by using a tighter pileup rejection criteria (7%) to reduce the contamination of events from different bunch crossings [47]. Additionally, the effect of magnetic field polarity of the ALICE's solenoid magnet is examined by repeating the analysis for both field polarities separately (13%). By default, both field polarities are combined in the final results. To evaluate systematic uncertainties in the track reconstruction, the selection on the minimum number of TPC space points is changed from 70 to 80 (8%), and the required χ^2 value per TPC cluster of the reconstruction fit is changed from [0.1, 2.5] to [0.1, 2.3] (7%). Furthermore, the applied threshold on the longitudinal DCA value of the reconstructed tracks is changed from 2 to 1 cm (7%). Finally, the default tracking selection is changed to another set of track-selection criteria, where the different conditions are set on the information from the ITS and TPC to yield flat azimuthal particle distribution (19%).

III. RESULTS

This section presents and discusses the SPC results. Section III A details the results as a function of centrality

for all studied observables. Section III B explores the interdependence among the SPC observables, while in Sec. III C, the SPC are compared with predictions from hydrodynamic models. Finally, Sec. III D compares the measurements with results from Pb-Pb collisions at $\sqrt{s_{NN}} = 2.76$ TeV [21]. Additional figures are provided in Appendixes A and C.

A. Comparison of magnitudes among various SPC

Figure 1 shows the two-harmonic SPC magnitudes as a function of centrality. The strongest magnitudes are obtained for $\langle \cos[4(\Psi_4 - \Psi_2)] \rangle$ in all centrality classes, with a clear increasing trend towards semicentral collisions. Other two-harmonic observables showing a similar trend are $\langle \cos[8(\Psi_4 - \Psi_2)] \rangle$, $\langle \cos[8(\Psi_8 - \Psi_2)] \rangle$, and $\langle \cos[6(\Psi_6 - \Psi_2)] \rangle$. Whereas $\langle \cos[8(\Psi_4 - \Psi_2)] \rangle$, $\langle \cos[4(\Psi_4 - \Psi_2)] \rangle$, and $\langle \cos[6(\Psi_6 - \Psi_2)] \rangle$ have slight decrease in trend at the most peripheral collisions, $\langle \cos[8(\Psi_8 - \Psi_2)] \rangle$ seems to saturate for centrality percentiles above 30%. For the aforementioned observables, the correlations come from the initial geometry and the nonlinear response of the medium. In central collisions, the correlations are weaker due to the more isotropic collision geometry. In semicentral collisions, the initial anisotropy causes stronger correlations, which are carried to the final state. The comparison with initial-state calculations is discussed in Sec. III C. The SPC $\langle \cos[6(\Psi_3 - \Psi_2)] \rangle$ and $\langle \cos[8(\Psi_8 - \Psi_4)] \rangle$ show no centrality dependence, with $\langle \cos[6(\Psi_3 - \Psi_2)] \rangle$ being compatible with zero with $n_\sigma = 2.07$ significance. The reported statistical significance, represented by the number n_σ of Gaussian standard deviations, is obtained from the p value of the χ^2 distribution. A strong magnitude in central and semicentral collisions with a decreasing trend towards peripheral collisions can be seen for $\langle \cos[6(\Psi_6 - \Psi_3)] \rangle$. The trend is slightly different from the other observables, and a possible explanation is discussed below.

In Ref. [21], it was noted that the magnitudes are associated with the number of correlating particles. The SPC measured with fewer-particle correlators have larger magnitudes. Similar results can be seen here, with a slight exception of the three-particle correlator $\langle \cos[8(\Psi_8 - \Psi_4)] \rangle$, for which the

correlation's lower magnitude is due to high-order symmetry plane, Ψ_8 . In addition, the magnitudes of SPC decrease both with the number of correlating particles and at higher orders. Triangular and higher-order flow in Pb-Pb collisions emerges from the granular distribution of colliding nucleons. These higher-ordered symmetries weaken due to the limited number of participating nucleons in the collision. This means that it becomes less likely for higher-order regular shapes, e.g., a shape with eight leaves, to develop persistently from one collision to another. Consequently, these symmetry planes become more difficult to detect and they exhibit weaker correlation strength. The number of correlated particles for a SPC ($\cos(a_1 n_1 \Psi_{n_1} + \dots + a_k n_k \Psi_{n_k})$) is $\sum a_i$ (note that $a_i > 0$). Furthermore, the reason for smaller magnitudes of correlators with fewer correlating particles could come from the fluctuations of flow-vector distributions. The particle correlators can be linked to the distribution of the flow-vector fluctuations [54,55], which result from the granular distribution of nucleons inside the colliding nuclei. According to the central limit theorem (CLT), the sample average of independent variables, i.e., the position of the nucleons in the overlapping region, approaches a Gaussian distribution. This was also noted in the SPC analysis at lower energies [21]. For distributions close to a Gaussian distribution, the higher-order moments (skewness, kurtosis, etc.) are weaker, and hence the higher-order correlators are weaker. In central collisions, the distributions tend to be more Gaussian than in peripheral collisions, which can be reflected in the ordering of the correlations in central collisions. The three-particle correlator $\langle \cos[6(\Psi_6 - \Psi_3)] \rangle$ is stronger than $\langle \cos[6(\Psi_6 - \Psi_2)] \rangle$ in central collisions. For the 20–30% centrality interval, the ordering begins to swap, as $\langle \cos[6(\Psi_6 - \Psi_2)] \rangle$ starts to show stronger correlations than $\langle \cos[6(\Psi_6 - \Psi_3)] \rangle$. This is due to the increasing deviations from Gaussian, causing higher moments to have more impact. Finally, it should be noted that a six-particle correlator $\langle \cos[8(\Psi_4 - \Psi_2)] \rangle$ has a large magnitude as it is the second moment of $\langle \cos[4(\Psi_4 - \Psi_2)] \rangle$. This will be discussed later in this section.

The results for three-harmonic SPC as a function of centrality are shown in Fig. 2. As in the case of two-harmonic SPC, the three-harmonic SPC also displays the ordering of the magnitudes strongly associated with the number of correlating particles. The largest magnitudes are shown by three-particle correlators, which are listed in order from the strongest to the weakest: $\langle \cos[2\Psi_2 + 3\Psi_3 - 5\Psi_5] \rangle$, $\langle \cos[2\Psi_2 + 4\Psi_4 - 6\Psi_6] \rangle$, $\langle \cos[2\Psi_2 + 5\Psi_5 - 7\Psi_7] \rangle$, $\langle \cos[3\Psi_3 + 4\Psi_4 - 7\Psi_7] \rangle$, and $\langle \cos[3\Psi_3 + 5\Psi_5 - 8\Psi_8] \rangle$. The magnitude ordering is described by the order of the symmetry planes, such that the weaker magnitudes are shown by the SPC with higher-order symmetry planes. Correlations among symmetry planes can be intuitively expected to arise from the cumulant expansion of harmonics [56–58], where higher-order harmonics have nonlinear contributions from the lower-order harmonics. The contributions contain a direct correlation between the participant planes, which can be expected to translate to the final state. This could be the reason why there is a positive correlation among symmetry planes Ψ_a , Ψ_b , and Ψ_c for which $na + mb = c$, where $n, m \in \mathbb{N}$. For example, a cumulant expansion of the fifth-order harmonic has contributions from

the second- and third-order harmonics, so SPC among Ψ_2 , Ψ_3 , and Ψ_5 , i.e., $\langle \cos[2\Psi_2 + 3\Psi_3 - 5\Psi_5] \rangle$, should have a strong correlation. The four-particle correlators, $\langle \cos[4\Psi_2 + 4\Psi_4 - 8\Psi_8] \rangle$ and $\langle \cos[4\Psi_2 + 3\Psi_3 - 7\Psi_7] \rangle$, as expected, have smaller magnitudes than the three-particle correlators with similar harmonics.

The observables $\langle \cos[2\Psi_2 - 6\Psi_3 + 4\Psi_4] \rangle$ and $\langle \cos[2\Psi_2 + 6\Psi_3 - 8\Psi_4] \rangle$ show negative correlation among the symmetry planes Ψ_2 , Ψ_3 , and Ψ_4 . Similarly, the symmetry planes Ψ_3 , Ψ_4 , and Ψ_5 are negatively correlated as shown in Fig. 2(c). The SPC analysis at $\sqrt{s_{NN}} = 2.76$ TeV also measured a negative correlation in $\langle \cos[2\Psi_2 - 6\Psi_3 + 4\Psi_4] \rangle$, whereas the others were not measured [21]. A similar negative correlation was seen among flow harmonics v_2 , v_3 , and v_4 in a paper that studied event-by-event correlations using higher-order SC in Pb-Pb collisions at $\sqrt{s_{NN}} = 2.76$ TeV [19]. However, the correlation among v_3 , v_4 , and v_5 was compatible with zero for SC. Furthermore, for three-harmonic SPC, the negative correlations are generally smaller in absolute magnitude than the positive correlations.

The lowest magnitude is shown by $\langle \cos[8\Psi_2 - 3\Psi_3 - 5\Psi_5] \rangle$. It is compatible with zero, having only a $n_\sigma = 0.82$ significance of a positive value. Although the correlation is minimal, it is slightly positive. A detailed view of this observable is presented in the model comparison section (Sec. III C) in Fig. 6.

The magnitudes of four-harmonic and the first-ever measured five-harmonic SPC as a function of centrality are displayed in Fig. 3. The five-harmonic SPC $\langle \cos[2\Psi_2 + 3\Psi_3 - 4\Psi_4 + 5\Psi_5 - 6\Psi_6] \rangle$ shows a small (if any) increase in magnitude towards semiperipheral collisions, where the correlation is positive within uncertainties. As observed with the two- and three-harmonic SPC, the trends vary among observables containing the same symmetry planes (Ψ_2 , Ψ_3 , Ψ_4 , Ψ_5). Specifically, $\langle \cos[2\Psi_2 - 3\Psi_3 - 4\Psi_4 + 5\Psi_5] \rangle$ and $\langle \cos[6\Psi_2 + 3\Psi_3 - 4\Psi_4 - 5\Psi_5] \rangle$ have positive magnitudes, while $\langle \cos[4\Psi_2 - 3\Psi_3 + 4\Psi_4 - 5\Psi_5] \rangle$ exhibits slightly negative correlations. The possible reason for this is discussed in Sec. III B, as well as the relatively strong correlation of the six-particle correlator $\langle \cos[6\Psi_2 + 3\Psi_3 - 4\Psi_4 - 5\Psi_5] \rangle$. A weak correlation is exhibited by $\langle \cos[4\Psi_2 + 6\Psi_3 - 4\Psi_4 - 6\Psi_6] \rangle$ with a weak centrality dependence. A strong centrality dependence is shown by $\langle \cos[2\Psi_2 - 4\Psi_4 - 5\Psi_5 + 7\Psi_7] \rangle$ even within the large uncertainties.

B. Observable interdependence

Many of the SPC observables presented in the previous section are built from different arrangements of the same symmetry planes. Due to the trigonometric properties of the cosine function, some of these results may trivially depend on each other. The starting point to probe the interdependence between two SPC is the following identity:

$$2 \cos(a) \cos(b) = \cos(a + b) + \cos(a - b). \quad (5)$$

Equation (5) states that if three out of the four cosine terms are known, the fourth term can be determined from the three known terms. In an experimental setting, one measures

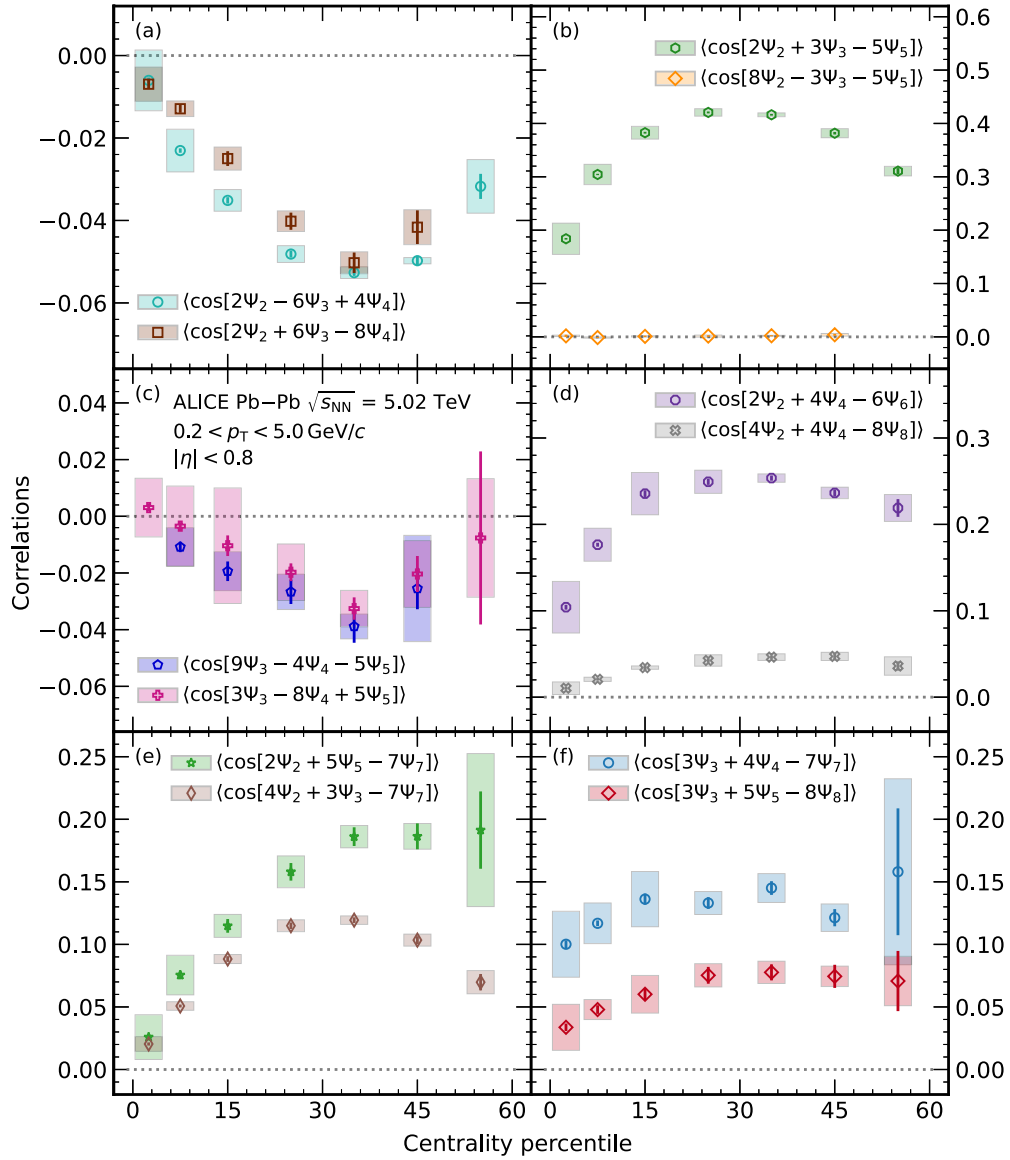


FIG. 2. Magnitude of SPC among three symmetry planes. The statistical and systematic uncertainties are depicted as lines and boxes, respectively.

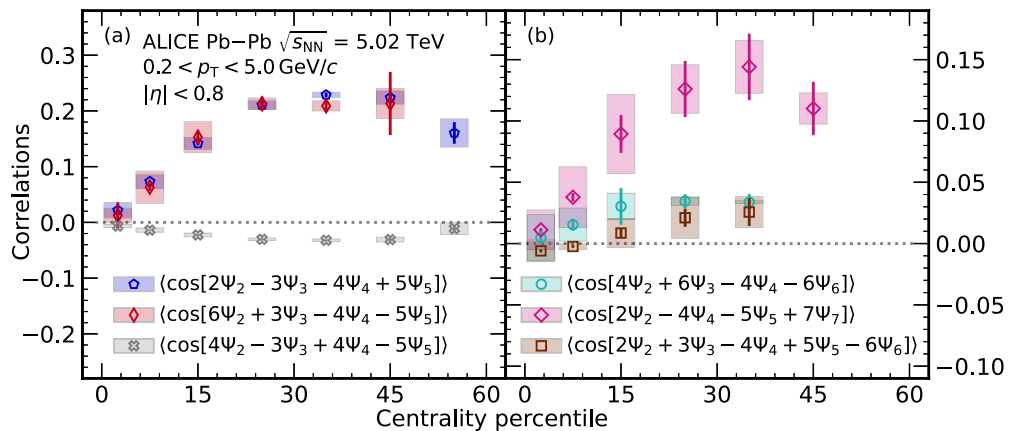


FIG. 3. Magnitude of SPC among four and five symmetry planes. The statistical and systematic uncertainties are depicted as lines and boxes, respectively.

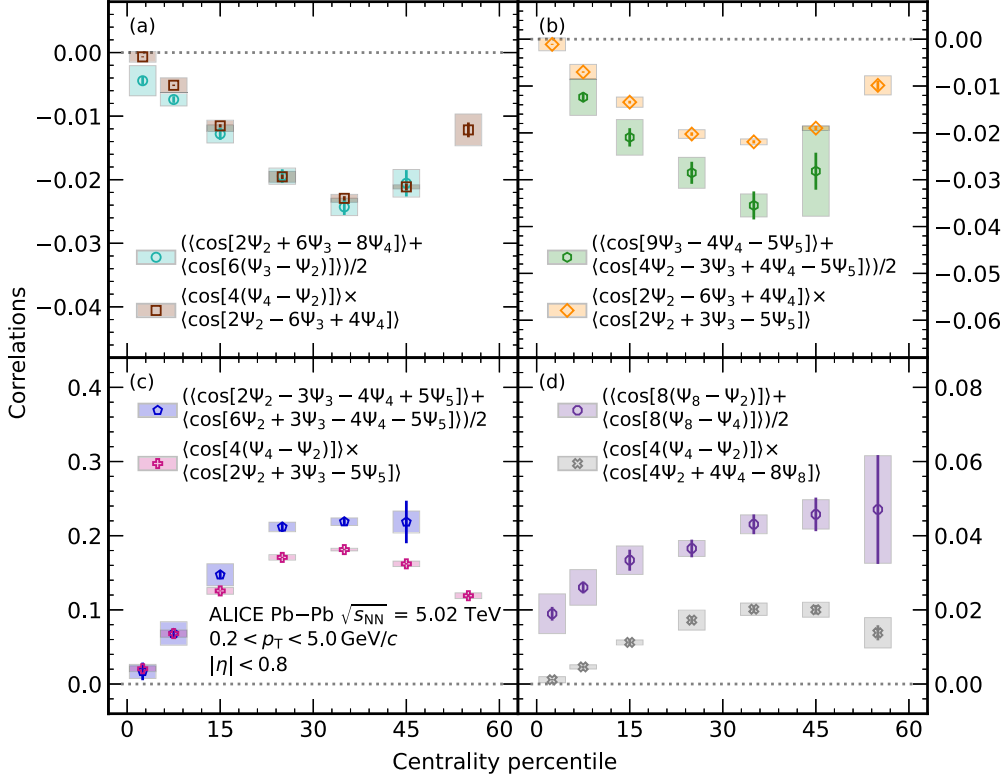


FIG. 4. Correlations between different sums of SPC compared with their respective products following Eq. (8), in the case of five different SPC. The statistical and systematic uncertainties are depicted as lines and boxes, respectively.

averages over all events and, thus, Eq. (5) becomes

$$2\langle\cos(a)\cos(b)\rangle = \langle\cos(a+b)\rangle + \langle\cos(a-b)\rangle. \quad (6)$$

If no direct correlation between $\cos(a)$ and $\cos(b)$ is assumed, the following approximation can be made:

$$\langle\cos(a)\rangle\langle\cos(b)\rangle \approx \langle\cos(a)\cos(b)\rangle. \quad (7)$$

Inserting Eq. (6) into Eq. (7) then gives

$$2\langle\cos(a)\rangle\langle\cos(b)\rangle \approx \langle\cos(a+b)\rangle + \langle\cos(a-b)\rangle. \quad (8)$$

Figure 4 presents the interdependence among five different combinations of harmonics through the correlations among different sums of SPC compared with their respective products. Panel (a) in Fig. 4 shows that the observed dependencies align well with the approximation given by Eq. (8), while panels (b)–(d) deviate from it. For panel (b), the $\langle\cos[2\Psi_2 - 6\Psi_3 + 4\Psi_4]\rangle$ and $\langle\cos[2\Psi_2 + 3\Psi_3 - 5\Psi_5]\rangle$ do not fully decorrelate in the form of Eq. (7), indicating a potential dependence or correlation between them. Since the approximation in Eq. (8) does not fully apply, this dependence does not fully explain the unexpected negative correlation observed for $\langle\cos[4\Psi_2 - 3\Psi_3 + 4\Psi_4 - 5\Psi_5]\rangle$, as discussed in Sec. III A. Nonetheless, the negative correlation could then result from the correlation between $\langle\cos[2\Psi_2 - 6\Psi_3 + 4\Psi_4]\rangle$ and $\langle\cos[2\Psi_2 + 3\Psi_3 - 5\Psi_5]\rangle$. In Sec. III A it was also noted that $\langle\cos[6\Psi_2 + 3\Psi_3 - 4\Psi_4 - 5\Psi_5]\rangle$ has a relatively large correlation. If the approximation in Eq. (8) could be applied with $\langle\cos[6\Psi_2 + 3\Psi_3 - 4\Psi_4 - 5\Psi_5]\rangle$, then the large correlation could be explained directly with the interdependence

of the other three harmonics found in the appliance of the approximation. However, it can be seen in panel (c) that the observables only follow the approximation from Eq. (8) in central collisions, but start disagreeing for centrality percentiles above 20%. As they do not agree in all centrality intervals, the cause for the large correlation cannot be explained fully by the interdependence. Finally in panel (d), the difference between left- and right-hand sides of Eq. (8) results from a correlation between $\langle\cos[4(\Psi_4 - \Psi_2)]\rangle$ and $\langle\cos[4\Psi_4 + 4\Psi_2 - 8\Psi_8]\rangle$.

To draw comprehensive conclusions, it is essential to quantify the correlations between different SPC observables. One potential approach is to measure the cumulants of symmetry plane correlations (CSC) defined in Ref. [38]. Nevertheless, the CSC in Ref. [38] pose strong requirements of correlating SPC to not share any symmetry planes, Ψ_n . For example, if SPC A is composed of symmetry planes Ψ_a and Ψ_b , and SPC B of Ψ_c and Ψ_d , then for CSC between SPC A and B it is required that $a, b \neq c, d$. These requirements are not satisfied with most observables presented in this subsection. Future studies are needed to address these correlations between SPC in depth and to check for less strict requirements in the CSC definition.

C. Comparison with models

These new experimental measurements of SPC are compared to predictions from two different state-of-the-art hydrodynamic models. The first model is the event-by-event

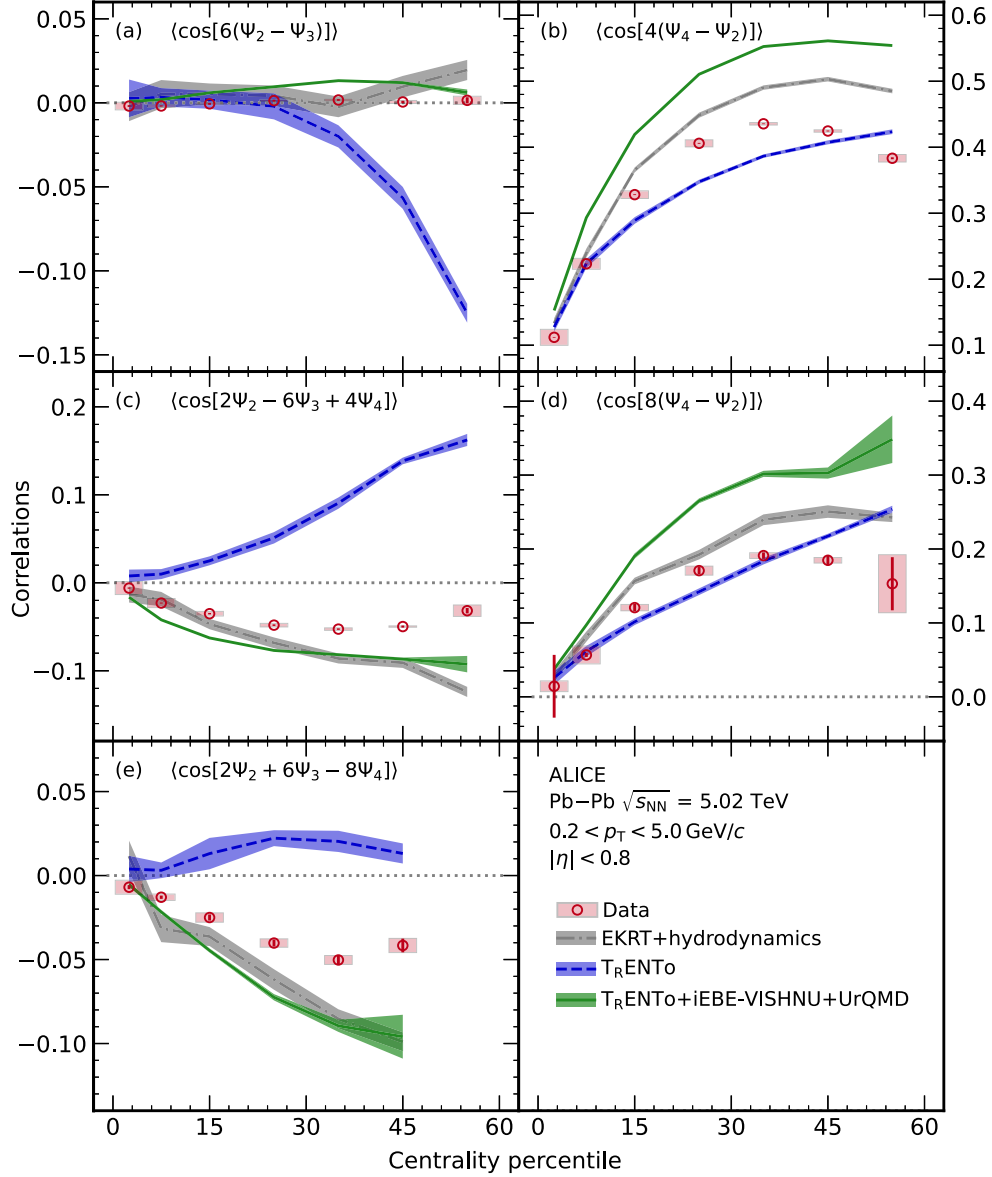


FIG. 5. Comparison of the centrality dependence of the correlations involving Ψ_2 , Ψ_3 , and Ψ_4 (red circles) with the theoretical predictions from $T_{\text{R}}\text{ENTo} + \text{iEBE-VISHNU} + \text{UrQMD}$ [63–66] and EKRT+hydrodynamics [60] shown as green and gray bands, respectively. Initial-state predictions from $T_{\text{R}}\text{ENTo}$ calculated with cumulant expansions are shown as blue bands. The lines (boxes) represent the statistical (systematic) uncertainties of the experimental data. The widths of the bands denote the statistical uncertainty of the model predictions.

EKRT+hydrodynamics [59,60], which combines next-to-leading order perturbative QCD and a saturation model [61,62] to determine the initial energy density profiles. The evolution of the QGP medium is described with viscous hydrodynamics, with a parametrization of the specific shear viscosity, $\eta/s(T) = \text{dyn}$, based on dynamical freeze-out conditions [60]. It is important to note that this model does not include a hadronic afterburner; instead the hadronic interactions and transport processes are carried out in the hydrodynamic framework that includes partial chemical freeze-out and dynamical kinetic freeze-out conditions. As such, the final-state predictions are derived directly with particles obtained at the hydrodynamic surface. The effect of hadronic interactions on SPC are discussed in detail in Appendix B. The calculations

presented in this paper were obtained with 10^5 events. The second model is $T_{\text{R}}\text{ENTo} + \text{VISH}(2+1) + \text{UrQMD}$ [63–66], referred to hereafter as $T_{\text{R}}\text{ENTo} + \text{iEBE-VISHNU} + \text{UrQMD}$. The $T_{\text{R}}\text{ENTo}$ model [67] is an initial-state model introduced to study high-energy nuclear collisions from pp to A-A systems. It is based on the use of a generalized mean of the nuclei’s energy density, with a free parameter whose value allows $T_{\text{R}}\text{ENTo}$ to reproduce the behavior of different models for initial conditions. Its output is then connected to the causal hydrodynamic evolution model, VISH(2+1) [66]. The hadronization and evolution of the final-state particles are described with the UrQMD model [63,64]. The free parameters of this hybrid model, like the initial conditions or QGP transport properties, were determined using the global Bayesian

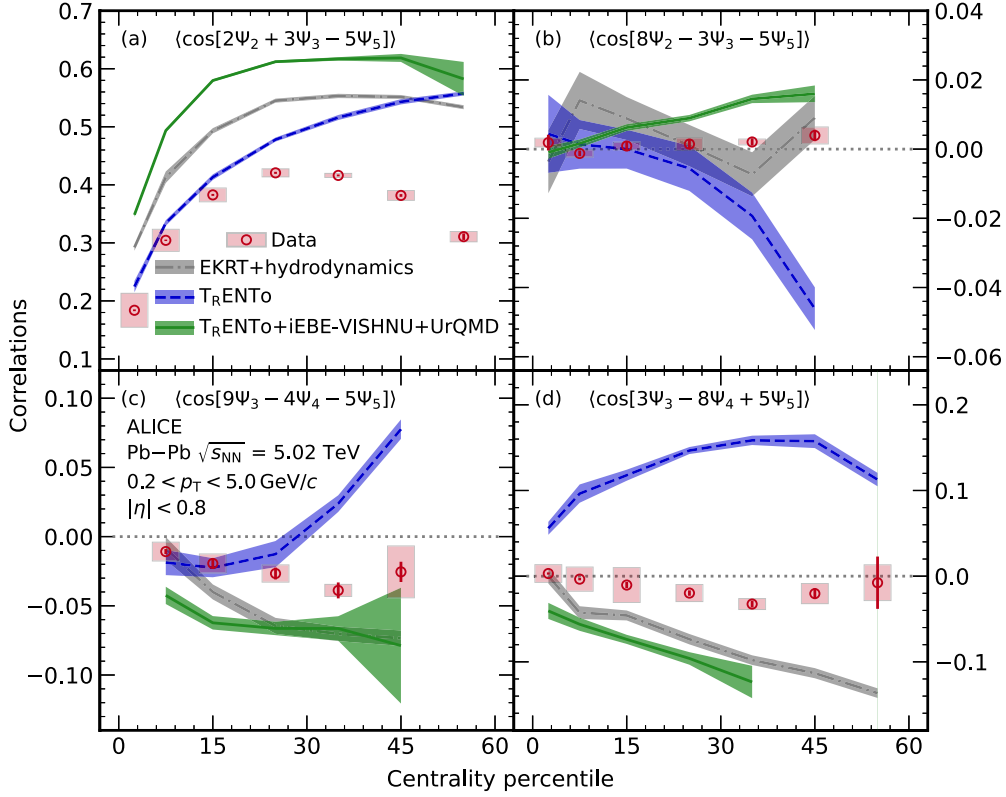


FIG. 6. Comparison of the centrality dependence of the three-harmonic correlations involving symmetry planes up to Ψ_5 (red circles) with the theoretical predictions from T_R ENTo+ iEBE-VISHNU+UrQMD [63–66] and EKRT+hydrodynamics [60] shown as green and gray bands, respectively. Initial-state predictions from T_R ENTo calculated with cumulant expansions are shown as blue bands. The lines (boxes) represent the statistical (systematic) uncertainties of the experimental data. The widths of the bands denote the statistical uncertainty of the model predictions.

analysis [9]. About 198 million events were simulated to extract the predictions presented in this paper. The initial-state calculations from T_R ENTo were obtained using one million generated events.

In heavy-ion collisions, the anisotropies in the final-state particle azimuthal distribution originate from the medium response to the anisotropies in the initial-state geometry. As in the final state, the asymmetries in the initial geometry can be described with a Fourier series, where the flow amplitudes v_n are replaced by the moments of the initial energy density, the eccentricities ε_n , and the symmetry planes Ψ_n by the participant planes Φ_n [68]. Another description of the initial geometry relies on the cumulants of the initial energy density. It was shown in Refs. [21,57,58] that the cumulant formulation leads to a more accurate representation of the asymmetric geometry. This is due to lower-order contributions in the higher-order eccentricities that are removed with the cumulant approach. As such, only the cumulant expansion is used in this study to extract the initial-state predictions. As an example, a cumulant expansion of fourth-order anisotropy can be expressed as

$$c_4 e^{i4\Phi_4} = \varepsilon_4 e^{i4\psi_4} + 3 \left(\frac{\langle r^2 \rangle^2}{\langle r^4 \rangle} \right) \varepsilon_2^2 e^{i4\psi_2}, \quad (9)$$

where ε describes the eccentricity of the initial energy density distribution and $\langle \dots \rangle$ defines an average with respect to the

energy density. In Eq. (9) Φ_n and ϕ_n are defined as participant planes in cumulant and moment expansions, respectively. For the lowest-order harmonics ($n < 4$) these are the same, while the higher-order cumulants start to differ from the moments due to their dependence on the lower-order eccentricities. Detailed descriptions of the cumulant and moment expansions can be found in Refs. [57,58]. In the following results, the initial-state predictions are obtained by evaluating correlations between participant planes, Φ_n , defined in the cumulant expansion. Due to the difference in magnitudes between initial- and final-state fluctuations, observables like the SC must be normalized to allow for proper comparisons between the different stages of the collisions. This procedure is not necessary for SPC, as the fluctuations of the flow amplitudes are already canceled out by the ratio in Eq. (4). Therefore, the correlations between participant planes and between symmetry planes of the same harmonics can straightforwardly be compared, allowing one to infer on the impact of the medium response on the initial-state correlations.

Figure 5 presents the correlations between two and three different symmetry planes involving Ψ_2 , Ψ_3 , and Ψ_4 , compared with predictions from both models. The absence of correlations between Ψ_2 and Ψ_3 [Fig. 5(a)] seen in the data is well reproduced by EKRT+hydrodynamics within uncertainties. The predictions from T_R ENTo+ iEBE-VISHNU+UrQMD also capture the flat centrality dependence of $\langle \cos[6(\Psi_3 -$

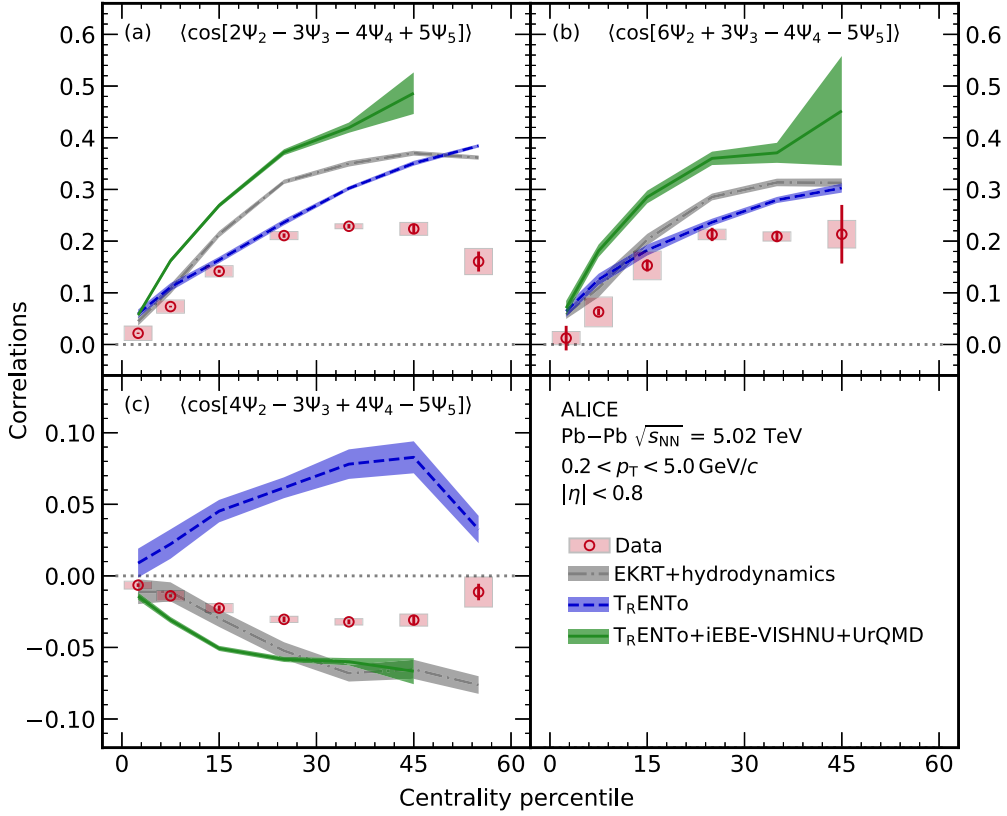


FIG. 7. Comparison of the centrality dependence of the correlations between different combinations of Ψ_2 , Ψ_3 , Ψ_4 , and Ψ_5 (red circles) with the theoretical predictions from $T_{\text{R}}\text{ENTo} + \text{iEBE-VISHNU} + \text{UrQMD}$ [63–66] and $\text{EKRT} + \text{hydrodynamics}$ [60] shown as green and gray bands, respectively. Initial-state predictions from $T_{\text{R}}\text{ENTo}$ calculated with cumulant expansions are shown as blue bands. The lines (boxes) represent the statistical (systematic) uncertainties of the experimental data. The widths of the bands denote the statistical uncertainty of the model predictions.

Ψ_2) but slightly overestimate the values. The latter confirms the outcome of the comparisons at lower energies discussed in Ref. [21]. In contrast, the initial-state predictions show a clear deviation from zero for centrality percentiles above 30%, indicating effects beyond linear hydrodynamic response for Ψ_2 and Ψ_3 . For the SPC between Ψ_2 and Ψ_4 in panels (b) and (d), both final-state calculations capture the trend but not the magnitude of the data. The calculations from $\text{EKRT} + \text{hydrodynamics}$ generally present less discrepancy with the experimental values, and both models show the best agreement with data in central collisions. As the linear response between Ψ_2 and Ψ_4 dominates for centralities up to 10% [69], the difference between data and model calculations in semicentral collisions may originate from the nonlinear coupling itself. Furthermore, the difference in magnitude between $\langle \cos[4(\Psi_4 - \Psi_2)] \rangle$ and $\langle \cos[8(\Psi_4 - \Psi_2)] \rangle$ is approximately reproduced by both models. Whereas the final-state predictions start to saturate, and even decrease, in the most peripheral collisions considered in this study, the initial-state predictions increase monotonically in the studied centrality range. Panels (c) and (e) show two different correlations of the three symmetry planes. Both models provide similar predictions and qualitatively reproduce the trend of the experimental data. As observed in the various two-harmonic SPC, data and models are in agreement within their respective uncertainties

in central collisions up to 20%. The initial-state predictions (obtained with $T_{\text{R}}\text{ENTo}$) are positive for both SPC, albeit with different centrality dependence, as opposed to the negative correlation observed for the final-state particles. Such behavior was already observed in the measurements by ALICE at $\sqrt{s_{NN}} = 2.76$ TeV [21], where the differences between the initial and final states were attributed to the hydrodynamic evolution of the system.

The correlations between three symmetry planes up to Ψ_5 are shown in Fig. 6, alongside their respective model calculations. The top panels present the SPC between Ψ_2 , Ψ_3 , and Ψ_5 . As in Fig. 5, the predictions from $\text{EKRT} + \text{hydrodynamics}$ better reproduce the data, although, both models drastically overestimate the magnitude of $\langle \cos[2\Psi_2 + 3\Psi_3 - 5\Psi_5] \rangle$. For both observables in the top panels, the trends of initial-state predictions are similar with the final-state predictions and the data in central collisions, but have large increases in the peripheral collisions. Panels (c) and (d) in Fig. 6 show $\langle \cos[9\Psi_3 - 4\Psi_4 - 5\Psi_5] \rangle$ and $\langle \cos[3\Psi_3 - 8\Psi_4 + 5\Psi_5] \rangle$, respectively, measured for the first time with the GE method. Similarly, as for the correlations between Ψ_2 , Ψ_3 , and Ψ_4 , the model calculations qualitatively describe the negative signature of the data. An interesting point to highlight is the difference in the behavior of the initial-state predictions from $T_{\text{R}}\text{ENTo}$ be-

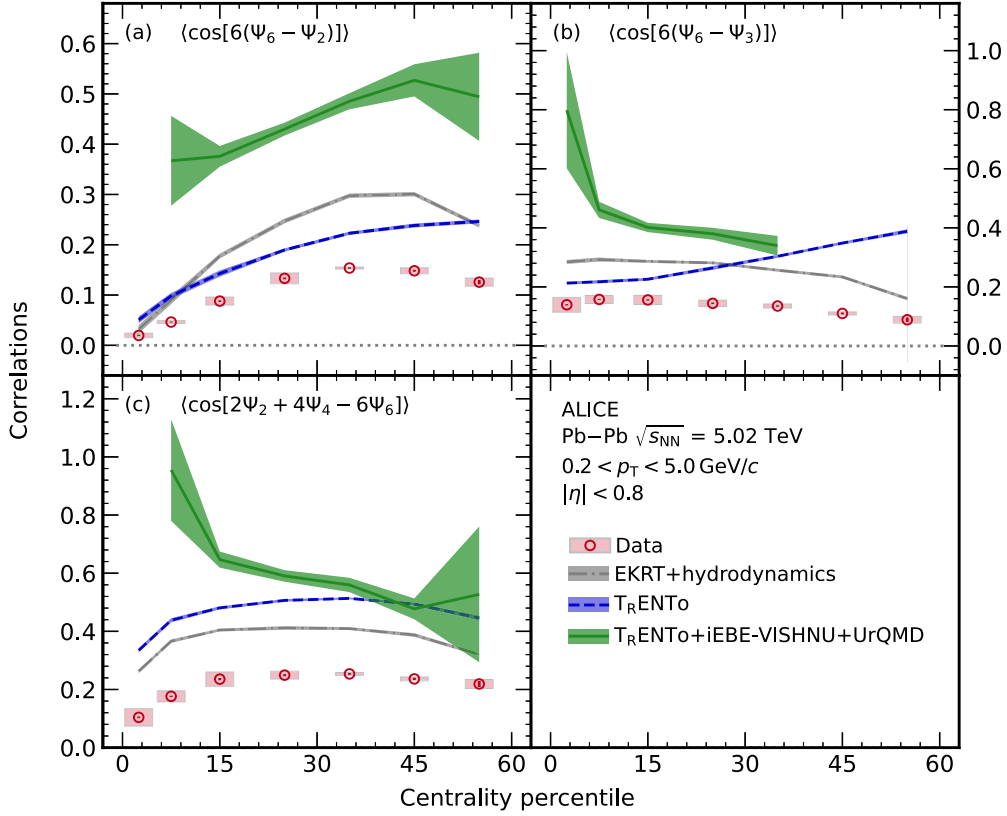


FIG. 8. Comparison of the centrality dependence of the correlations involving symmetry planes up to Ψ_6 (red circles) with the theoretical predictions from T_R ENTo+iEBE-VISHNU+UrQMD [63–66] and EKRT+hydrodynamics [60] shown as green and gray bands, respectively. Initial-state predictions from T_R ENTo calculated with cumulant expansions are shown as blue bands. The lines (boxes) represent the statistical (systematic) uncertainties of the experimental data. The widths of the bands denote the statistical uncertainty of the model predictions.

tween the two observables. While $\langle \cos[9\Psi_3 - 4\Psi_4 - 5\Psi_5] \rangle$ is negative and agrees with the data in central collisions, it strongly increases to positive values in more peripheral events. This is in contrast with the initial-state predictions for $\langle \cos[3\Psi_3 - 8\Psi_4 + 5\Psi_5] \rangle$ that are positive in all centralities. Such difference can be explained by the respective cumulant expansions of both SPC, where $\langle \cos[3\Psi_3 - 8\Psi_4 + 5\Psi_5] \rangle$ contains additional correlations between the second-, third-, fourth-, and fifth-order participant planes.

Three different correlations between Ψ_2 , Ψ_3 , Ψ_4 , and Ψ_5 can be seen in Fig. 7. The SPC $\langle \cos[2\Psi_2 - 3\Psi_3 - 4\Psi_4 + 5\Psi_5] \rangle$ and $\langle \cos[6\Psi_2 + 3\Psi_3 - 4\Psi_4 - 5\Psi_5] \rangle$ shown in panels (a) and (b), respectively, have similar magnitude and centrality dependence for model predictions and data. Both calculations, T_R ENTo+iEBE-VISHNU+UrQMD and EKRT+hydrodynamics, reproduce the centrality dependence of the experimental values but not their magnitude. The predictions from EKRT+hydrodynamics are, as seen previously, closer to the data and in agreement with them within uncertainties for the 0–20% centrality interval. This range also corresponds to the one where the initial-state calculations from T_R ENTo are in agreement with the data, but not with the final-state results from T_R ENTo+iEBE-VISHNU+UrQMD.

Finally, the results for $\langle \cos[4\Psi_2 - 3\Psi_3 + 4\Psi_4 - 5\Psi_5] \rangle$ shown in panel (c) of Fig. 7 present the most striking

differences with the $\langle \cos[2\Psi_2 - 3\Psi_3 - 4\Psi_4 + 5\Psi_5] \rangle$ and $\langle \cos[6\Psi_2 + 3\Psi_3 - 4\Psi_4 - 5\Psi_5] \rangle$. While the initial-state predictions are still positive, the final-state results for both the models and the experimental measurements are negative. As discussed in Sec. III B, this observable is expected to be consistent with zero but obtains negative magnitude due to correlations between $\langle \cos[2\Psi_2 - 6\Psi_3 + 4\Psi_4] \rangle$ and $\langle \cos[2\Psi_2 + 3\Psi_3 - 5\Psi_5] \rangle$.

Figure 8 gathers the model predictions for the two- and three-harmonic SPC involving up to Ψ_6 . Both final-state models manage to capture the trend but not the magnitude of the data. The initial-state predictions show similar trend as the final-state predictions for $\langle \cos[6(\Psi_6 - \Psi_2)] \rangle$ and $\langle \cos[2\Psi_2 + 4\Psi_4 - 6\Psi_6] \rangle$, while the initial- and final-state predictions for $\langle \cos[6(\Psi_6 - \Psi_3)] \rangle$ have opposite trends. The increasing and decreasing trends of initial- and final-state predictions for $\langle \cos[6(\Psi_6 - \Psi_3)] \rangle$ were also noted in the lower energy analysis in Ref. [21].

D. Beam energy dependence

Figure 9 shows different two- and three-harmonic SPC compared with the measurements in Pb–Pb collisions at $\sqrt{s_{NN}} = 2.76$ TeV [21], along with the EKRT+hydrodynamic model predictions at the two collision energies. No significant energy dependence is observed for

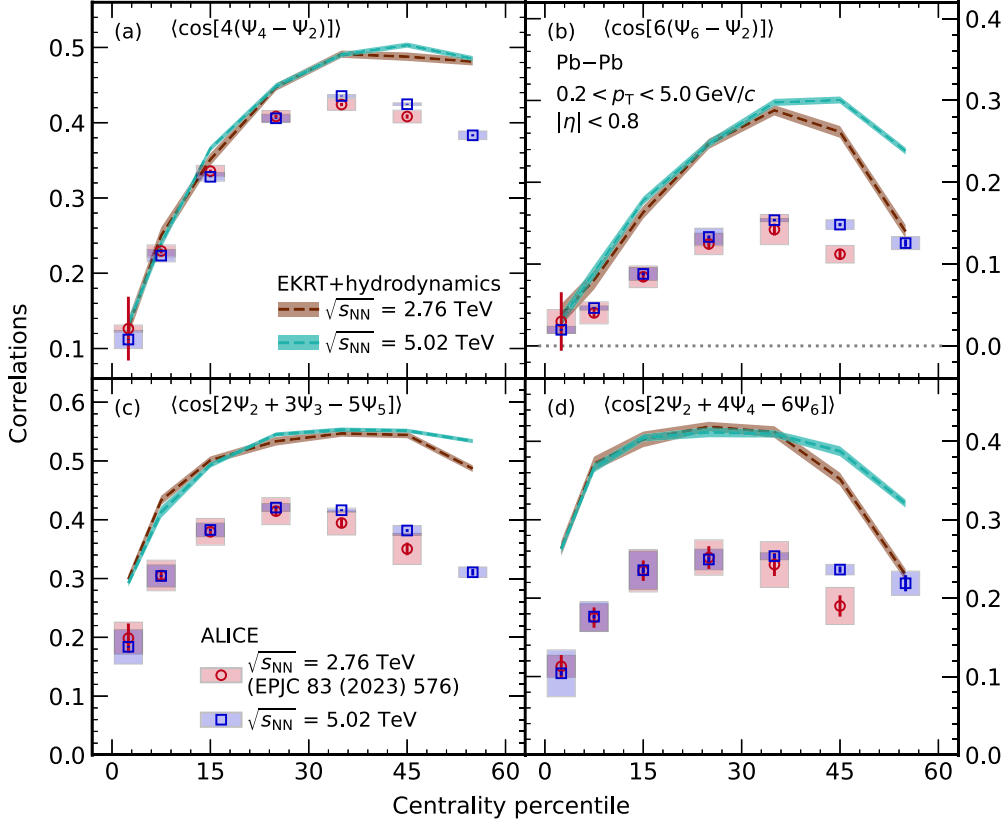


FIG. 9. Comparison of different two- and three-harmonic SPC measured at $\sqrt{s_{NN}} = 2.76$ TeV (red circles) [21] and at $\sqrt{s_{NN}} = 5.02$ TeV (blue squares) by ALICE. The results are compared with the predictions from EKRT+hydrodynamics [60] at the same center-of-mass energies (brown and green bands, respectively). The lines (boxes) represent the statistical (systematic) uncertainties in the experimental data. The widths of the bands denote the statistical uncertainty of the model predictions.

the data as the SPC at different beam energies agree with each other within 1.1σ over the full centrality range (for more details, see Appendix C). However, when checking in more detail the evolution with centrality, the four different combinations of SPC shown in Fig. 9 present an interesting behavior for both the experimental data and the calculations from EKRT+hydrodynamics.

In all four cases, the results at both energies are in good agreement for centralities up to 40%. Beyond this centrality, the magnitudes of the SPC measured at higher beam energy tend to be slightly larger, even though strong conclusions cannot be drawn considering the current uncertainties. A difference in the same direction and with more pronounced magnitude is seen also in the model predictions. This trend suggests that the longer duration of the QGP phase in Pb-Pb collisions at higher center-of-mass energy may be a contributing factor in the lesser dissipation of the correlations when compared to the ones at lower beam energies [70,71].

IV. SUMMARY

This article presents the measurements of the correlations between different symmetry planes in Pb-Pb collisions at $\sqrt{s_{NN}} = 5.02$ TeV using the recently developed Gaussian estimator technique, which allows one to eliminate the bias in previously used estimators stemming from correlated flow

amplitudes. The larger data sample allows the analysis to be extended by including more combinations of harmonics than previously reported in Pb-Pb collisions at $\sqrt{s_{NN}} = 2.76$ TeV [21]. Furthermore, the first measurement of the correlations between five different symmetry planes is shown. The investigation of the centrality dependence of the various symmetry plane correlations (SPC) confirms the influence of the order of the SPC and the collision centrality on the correlation strength. In addition, for every harmonic-order SPC, the number of correlating particles has a considerable impact on the hierarchy of the correlation strength as seen previously in the results at $\sqrt{s_{NN}} = 2.76$ TeV. No significant energy dependence is observed within the uncertainties at the comparison of the present data with the measurements at the lower center-of-mass energy. The measured results are compared with state-of-the-art hydrodynamic model calculations. These calculations qualitatively describe the data showing large differences for correlators exhibiting a significant non-linear response of the medium to initial-state geometry. The EKRT+hydrodynamic model is in better agreement with the data than the $T_{\text{RENT}}\text{o} + \text{iEBE-VISHNU} + \text{UrQMD}$ model, especially for correlations involving Ψ_2 and Ψ_4 . This disagreement between the models can partially be explained with the effects of hadronic afterburner that is included in $T_{\text{RENT}}\text{o} + \text{iEBE-VISHNU} + \text{UrQMD}$ but is absent in EKRT+hydrodynamics. Nevertheless, deviations from the

data are observed in both models, mainly for peripheral collisions. The correlations between different symmetry planes offer insights into the impact of the medium response on initial-state correlations. The comparisons indicate that the models tend to overestimate the experimental values, possibly due to factors such as the nonlinear response from the initial state to the final state or the use of inaccurate parameters. More specifically, the EKRT and iEBE-VISHNU with $T_{\text{R}}\text{ENTo}$ framework exhibit distinct characteristics in their initial-state correlations and subsequent hydrodynamic evolution. These discrepancies provide constraints for refining both initial condition parameters and final-state evolution in heavy-ion collision models. The interplay between the initial conditions and hydrodynamic response, thus, becomes visible in results as deviations from experimental measurements. The SPC's sensitivity to model parameters not only constrains the QGP parameters, but also helps us understand the underlying physics at each stage of the heavy ion collision and how these stages combine.

In conclusion, this study provides valuable insights into the correlations between symmetry planes in heavy-ion collisions and highlights the need for further improvements in modeling the QCD matter properties in ultrarelativistic heavy-ion collisions.

ACKNOWLEDGMENTS

The ALICE Collaboration would like to thank Henry Hirvonen for providing the latest predictions from the state-of-the-art hydrodynamic model, event-by-event EKRT+hydrodynamics. The ALICE Collaboration would like to thank all its engineers and technicians for their invaluable contributions to the construction of the experiment and the CERN accelerator teams for the outstanding performance of the LHC complex. The ALICE Collaboration gratefully acknowledges the resources and support provided by all Grid centres and the Worldwide LHC Computing Grid (WLCG) Collaboration. The ALICE Collaboration acknowledges the following funding agencies for their support in building and running the ALICE detector: A. I. Alikhanyan National Science Laboratory (Yerevan Physics Institute) Foundation (ANSL), State Committee of Science, and World Federation of Scientists (WFS), Armenia; Austrian Academy of Sciences, Austrian Science Fund (FWF): [M 2467-N36] and Nationalstiftung für Forschung, Technologie und Entwicklung, Austria; Ministry of Communications and High Technologies, National Nuclear Research Center, Azerbaijan; Conselho Nacional de Desenvolvimento Científico e Tecnológico (CNPq), Financiadora de Estudos e Projetos (Finep), Fundação de Amparo à Pesquisa do Estado de São Paulo (FAPESP), and Universidade Federal do Rio Grande do Sul (UFRGS), Brazil; Bulgarian Ministry of Education and Science, within the National Roadmap for Research Infrastructures 2020–2027 (object CERN), Bulgaria; Ministry of Education of China (MOEC), Ministry of Science & Technology of China (MSTC), and National Natural Science Foundation of China (NSFC), China; Ministry of Science and Education and Croatian Science Foundation,

Croatia; Centro de Aplicaciones Tecnológicas y Desarrollo Nuclear (CEADEN), Cubaenergía, Cuba; The Ministry of Education, Youth and Sports of the Czech Republic, Czech Republic; The Danish Council for Independent Research | Natural Sciences, the VILLUM FONDEN, and Danish National Research Foundation (DNRF), Denmark; Helsinki Institute of Physics (HIP), Finland; Commissariat à l’Energie Atomique (CEA) and Institut National de Physique Nucléaire et de Physique des Particules (IN2P3) and Centre National de la Recherche Scientifique (CNRS), France; Bundesministerium für Bildung und Forschung (BMBF) and GSI Helmholtzzentrum für Schwerionenforschung GmbH, Germany; General Secretariat for Research and Technology, Ministry of Education, Research and Religions, Greece; National Research, Development and Innovation Office, Hungary; Department of Atomic Energy Government of India (DAE), Department of Science and Technology, Government of India (DST), University Grants Commission, Government of India (UGC), and Council of Scientific and Industrial Research (CSIR), India; National Research and Innovation Agency - BRIN, Indonesia; Istituto Nazionale di Fisica Nucleare (INFN), Italy; Japanese Ministry of Education, Culture, Sports, Science and Technology (MEXT) and Japan Society for the Promotion of Science (JSPS) KAKENHI, Japan; Consejo Nacional de Ciencia (CONACYT) y Tecnología, through Fondo de Cooperación Internacional en Ciencia y Tecnología (FONCICYT) and Dirección General de Asuntos del Personal Académico (DGAPA), Mexico; Nederlandse Organisatie voor Wetenschappelijk Onderzoek (NWO), Netherlands; The Research Council of Norway, Norway; Pontificia Universidad Católica del Perú, Peru; Ministry of Science and Higher Education, National Science Centre and WUT ID-UB, Poland; Korea Institute of Science and Technology Information and National Research Foundation of Korea (NRF), Republic of Korea; Ministry of Education and Scientific Research, Institute of Atomic Physics, Ministry of Research and Innovation, and Institute of Atomic Physics and Universitatea Nationala de Stiinta si Tehnologie Politehnica Bucuresti, Romania; Ministry of Education, Science, Research and Sport of the Slovak Republic, Slovakia; National Research Foundation of South Africa, South Africa; Swedish Research Council Formas (VR) and Knut and Alice Wallenberg Foundation (KAW), Sweden; European Organization for Nuclear Research, Switzerland; Suranaree University of Technology (SUT), National Science and Technology Development Agency (NSTDA), and National Science, Research and Innovation Fund (NSRF via PMU-B B05F650021), Thailand; Turkish Energy, Nuclear and Mineral Research Agency (TENMAK), Turkey; National Academy of Sciences of Ukraine, Ukraine; Science and Technology Facilities Council (STFC), United Kingdom; National Science Foundation of the United States of America (NSF) and United States Department of Energy, Office of Nuclear Physics (DOE NP), United States of America. In addition, individual groups or members have received support from Czech Science Foundation (Grant No. 23-07499S), Czech Republic; FORTE project, Reg. No. CZ.02.01.01/00/22_008/0004632, Czech Republic, co-funded by the European Union, Czech Republic; European

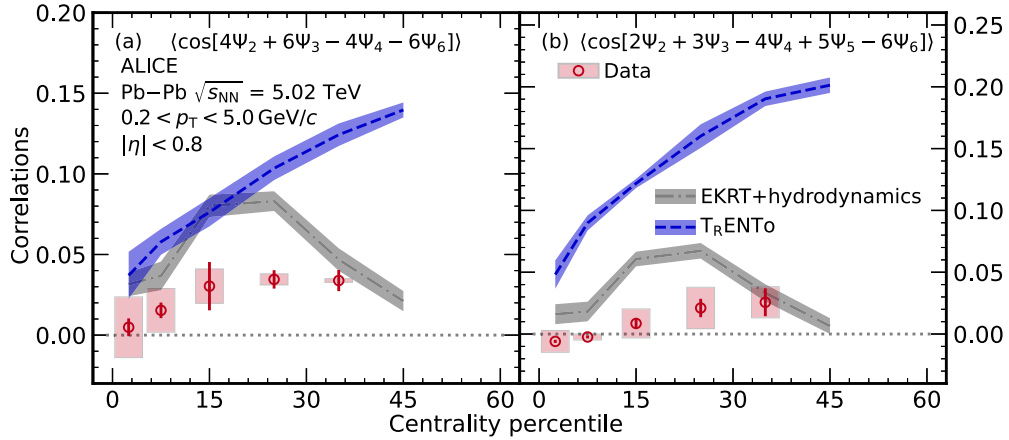


FIG. 10. Comparison of the centrality dependence of the correlations among different combinations of Ψ_2 , Ψ_3 , Ψ_4 , Ψ_5 , and Ψ_6 (red circles) with the theoretical predictions from EKRT+hydrodynamics [60] shown in gray bands. Initial-state predictions from T_RENTo [63–66] calculated with cumulant expansions are shown as blue bands. The lines (boxes) represent the statistical (systematic) uncertainties in the experimental data. The widths of the bands denote the statistical uncertainty of the model predictions.

Research Council (Grant No. 950692), European Union; ICSC–Centro Nazionale di Ricerca in High Performance Computing, Big Data and Quantum Computing, European Union–NextGenerationEU; Academy of Finland (Center of Excellence in Quark Matter) (Grants No. 346327, and No. 346328), Finland.

APPENDIX A: FURTHER MODEL COMPARISONS

This Appendix presents observables not shown in Figs. 5–8 compared with model calculations. Due to their large uncertainties, no final-state calculations from T_RENTo+ iEBE-VISHNU+UrQMD are presented in Figs. 10–12.

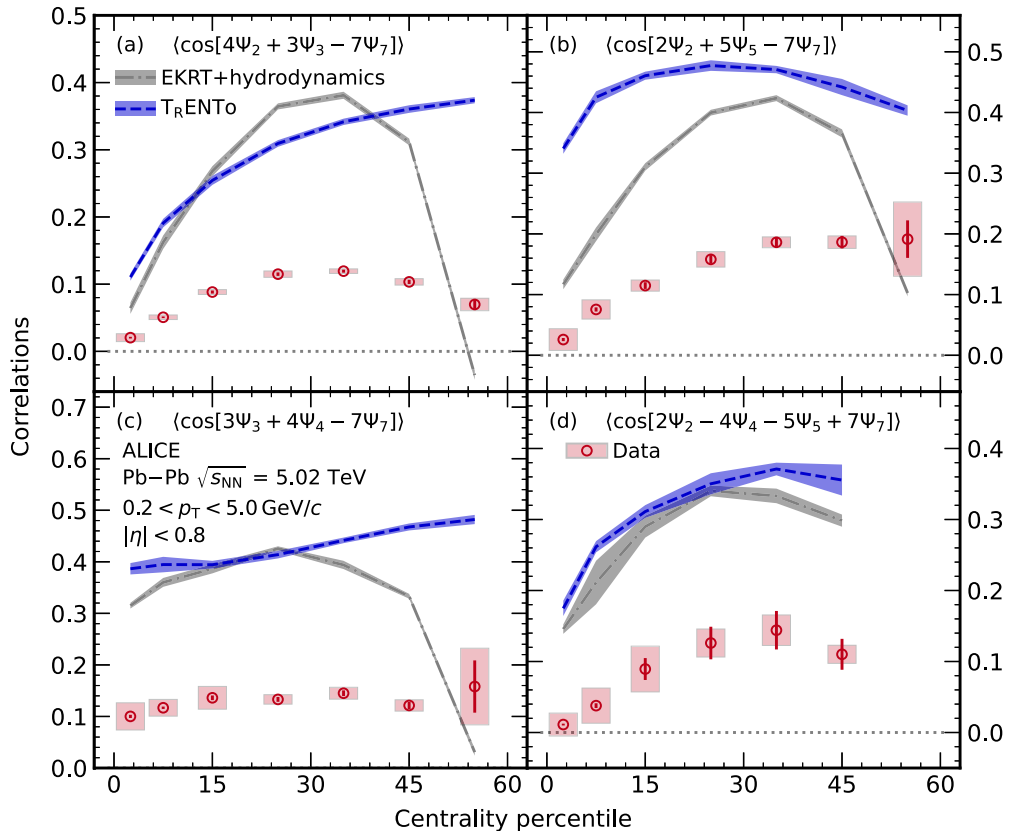


FIG. 11. Comparison of the centrality dependence of the correlations between different combinations of SPC involving planes up to Ψ_7 (red circles) with the theoretical predictions from EKRT+hydrodynamics [60] shown in gray bands. Initial-state predictions from T_RENTo [63–66] calculated with cumulant expansions are shown as blue bands. The lines (boxes) represent the statistical (systematic) uncertainties in the experimental data. The widths of the bands denote the statistical uncertainty of the model predictions.

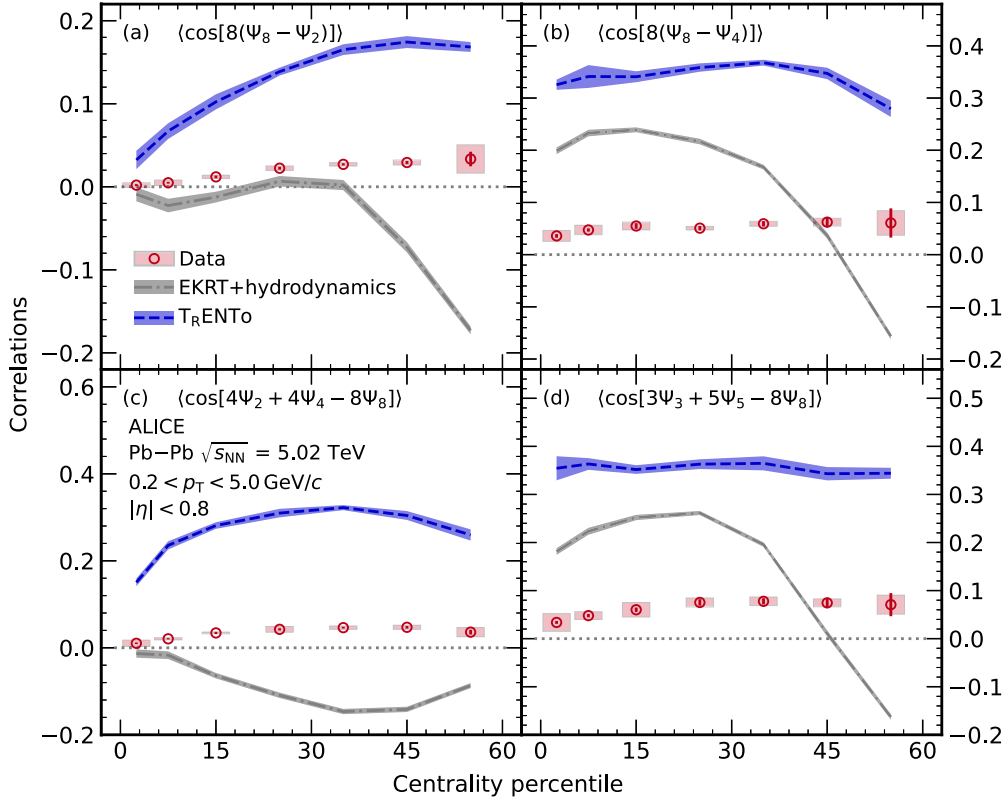


FIG. 12. Comparison of the centrality dependence of the correlations between different combinations including Ψ_8 (red circles) with the theoretical predictions from EKRT+hydrodynamics [60] shown in gray bands. Initial-state predictions from $T_R ENT o$ [63–66] calculated with cumulant expansions are shown as blue bands. The lines (boxes) represent the statistical (systematic) uncertainties of the experimental data. The widths of the bands denote the statistical uncertainty of the model predictions.

Additional combinations involving the symmetry planes Ψ_2 , Ψ_3 , Ψ_4 , Ψ_5 , and Ψ_6 can be seen in Fig. 10, including the first measured five-harmonic SPC among those planes. Contrary to the previous observations, the predictions from EKRT+hydrodynamics not only overestimate the data but also do not manage to reproduce their centrality dependence. The complexity of the interplay between the nonlinear response of Ψ_5 and Ψ_6 may be the cause of such a discrepancy. This confirms the need for higher-order observables to adjust the parameters in the theoretical models as well as the need for the improvement of the models themselves. Furthermore, the comparison of the initial-state predictions from $T_R ENT o$ with the experimental data hints at a dampening of the initial state correlations, especially in more peripheral collisions. This might be due to a non-negligible nonlinear response, which has to be addressed by future studies.

Figures 11 and 12 show results for four different SPC involving Ψ_7 and Ψ_8 , respectively. As for the results in Fig. 10, the predictions from EKRT+hydrodynamics [60] cannot reproduce the centrality dependence of the experimental values. Interestingly, the calculations in Figs. 11(a)–11(c) and in Figs. 12(a), 12(b), and 12(d) all present similar strongly decreasing signals for centrality percentiles above 40% for the cases involving Ψ_7 and above 30% of centrality for Ψ_8 . In general, a decrease of correlation strength is expected in the transition from semicentral to peripheral collisions as the QCD medium produced becomes less thermalised.

Thus, initial-state correlations are not properly transferred into the final-state momentum space, leading to the observed decrease in the correlation strength. Note that the decrease of correlation strength towards peripheral collisions seems in general to occur faster in the EKRT+hydrodynamics predictions than in the data, which could indicate a less thermalized medium in the model predictions. As the predictions from EKRT+hydrodynamics are extracted at the hydrodynamic surface and, thus, do not contain separate hadronic transport models, further studies are required in that direction.

APPENDIX B: EFFECT OF HADRONIC INTERACTIONS

In model comparison section (Sec. III), a quantitative difference was found between EKRT+hydrodynamics and $T_R ENT o + iEBE-VISHNU + UrQMD$, which could be caused by a lack of hadronic afterburner model in the former. To quantify the effects of hadronic interactions on SPC, model set $T_R ENT o + iEBE-VISHNU + UrQMD$ is run without UrQMD and the results are compared. Figure 13 displays the model outcomes of $T_R ENT o + iEBE-VISHNU + UrQMD$ and $T_R ENT o + iEBE-VISHNU$, which are compared with the EKRT+hydrodynamics and experimental results. A clear distinction in the magnitude between $T_R ENT o + iEBE-VISHNU$ with and without UrQMD is shown for $\langle \cos[4(\Psi_4 - \Psi_2)] \rangle$ and $\langle \cos[2\Psi_2 + 3\Psi_3 - 5\Psi_5] \rangle$. For these observables the $T_R ENT o + iEBE-VISHNU$ predictions are of similar order

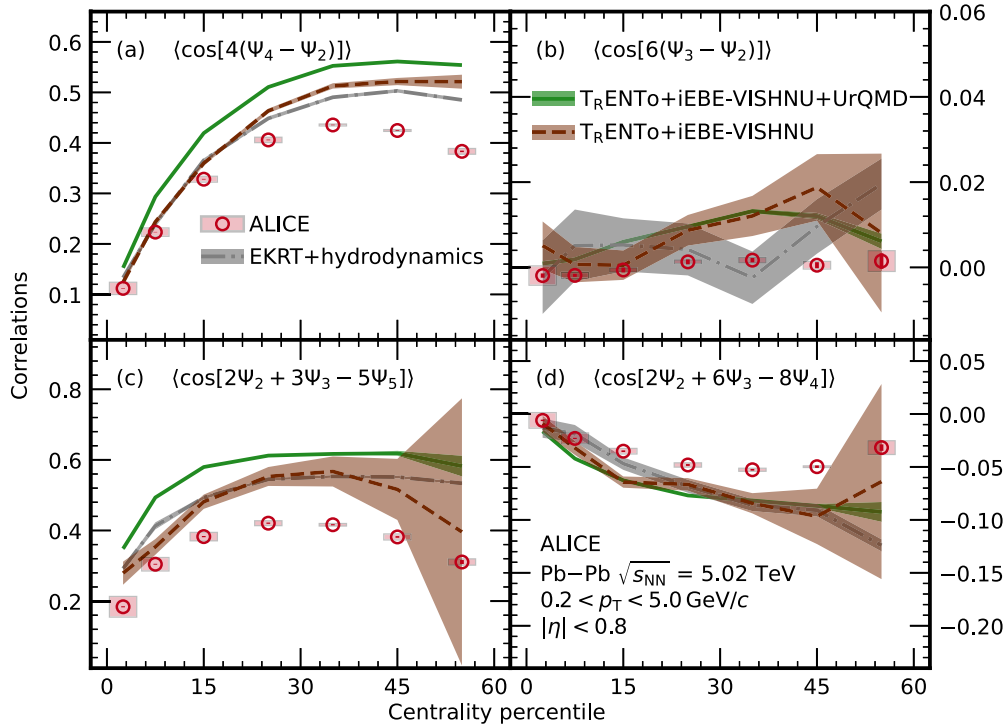


FIG. 13. Comparison of predictions from models with and without hadronic cascade for a few selected SPC observables. The theoretical predictions from EKRT+hydrodynamics [60] are shown in gray bands, $T_{\text{R}}\text{ENTo}+i\text{EBE-VISHNU}+\text{UrQMD}$ in green bands, and $T_{\text{R}}\text{ENTo}+i\text{EBE-VISHNU}$ in brown bands. The experimental data are shown as red circles with the lines (boxes) representing the statistical (systematic) uncertainties. The widths of the bands denote the statistical uncertainty of the model predictions.

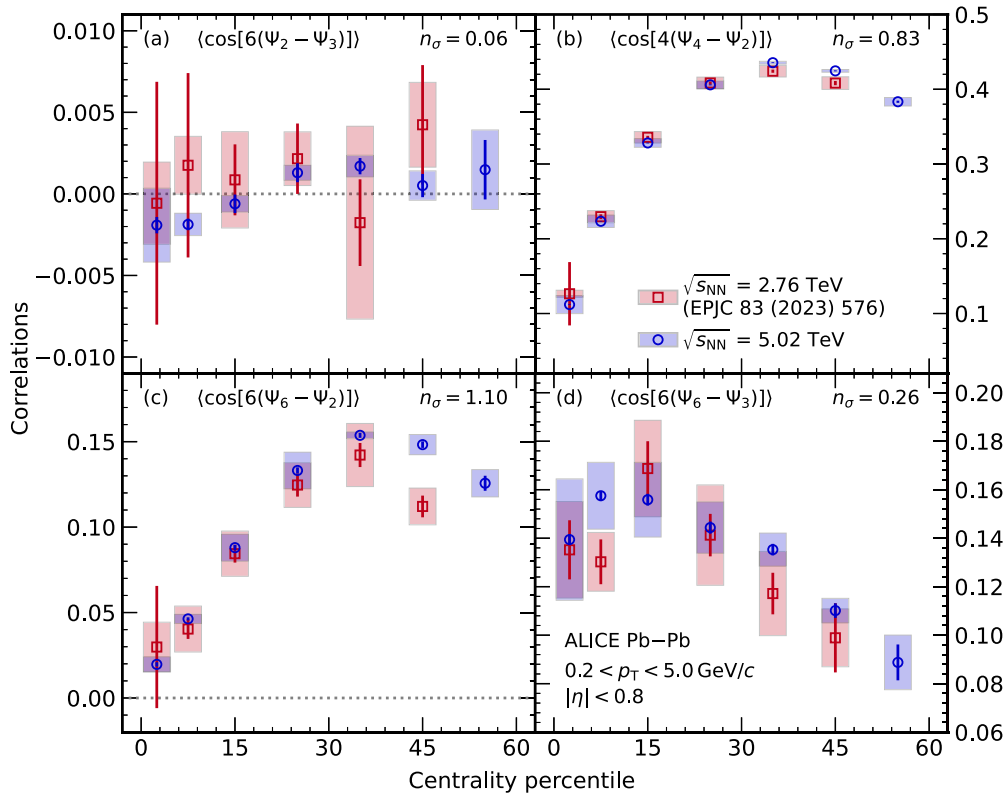


FIG. 14. Correlations between two different symmetry planes measured at $\sqrt{s_{NN}} = 2.76$ TeV (red squares) from [21] and $\sqrt{s_{NN}} = 5.02$ TeV (blue circles). The lines (boxes) represent the statistical (systematic) uncertainties. The agreement between the two sets of data is indicated with its number of σ at the top right of each panel.

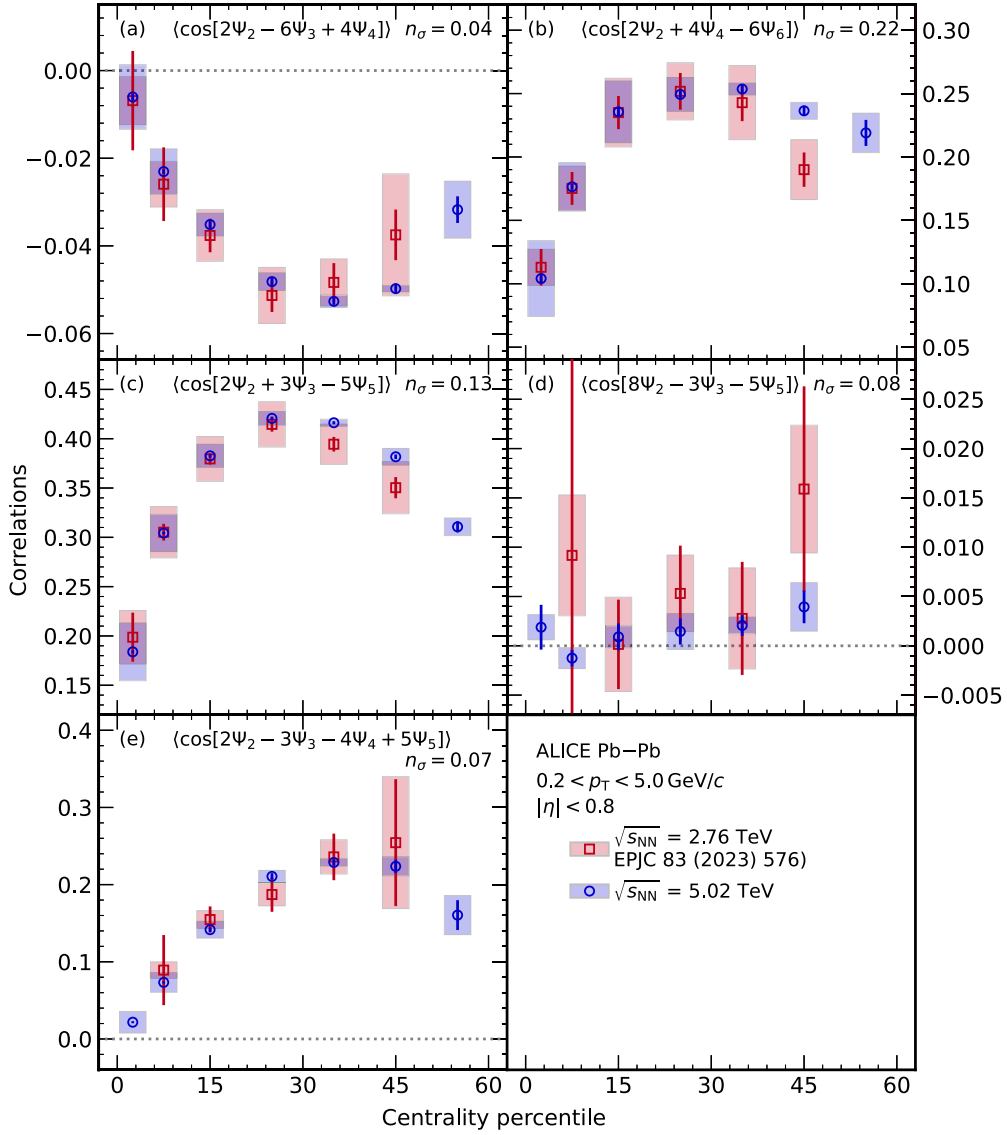


FIG. 15. Correlations between three and four different symmetry planes measured at $\sqrt{s_{NN}} = 2.76$ TeV (red squares) from [21] and $\sqrt{s_{NN}} = 5.02$ TeV (blue circles). The lines (boxes) represent the statistical (systematic) uncertainties. The agreement between the two sets of data is indicated with its number of σ at the top right of each panel.

with EKRT+hydrodynamics and, hence, in better agreement with the data. For $\langle \cos[6(\Psi_3 - \Psi_2)] \rangle$ and $\langle \cos[2\Psi_2 + 6\Psi_3 - 8\Psi_4] \rangle$ the hadronic interactions do not increase the magnitude, and the predictions from all three models are in a better agreement. As such, the difference between $T_{R}ENTo+ iEBE-VISHNU+UrQMD$ and EKRT+hydrodynamics can be partially explained with inclusion of a hadronic cascade model in the former. Nevertheless strong conclusions cannot be made because for $T_{R}ENTo+ iEBE-VISHNU+UrQMD$ and EKRT+hydrodynamics the model parameters are tuned to represent experimental data, mainly particle yields, anisotropic flow, and mean transverse momentum distributions. Here $T_{R}ENTo+ iEBE-VISHNU$ predictions are evaluated with same parametrization as for $T_{R}ENTo+ iEBE-VISHNU+UrQMD$, and with that parametrization the model does not reproduce the aforementioned experimental data. On average, the model produces fewer particles with higher trans-

verse momentum when run without UrQMD. The parameter optimization for the model without UrQMD is beyond the scope of this paper. Hadronic interactions play an important role in modeling heavy-ion collisions, but a more detailed analysis is needed to fully conclude their effects.

APPENDIX C: COMPARISON WITH RESULTS AT LOWER BEAM ENERGY

Figures 14 and 15 display the comparison between the present results from Pb-Pb collisions at $\sqrt{s_{NN}} = 5.02$ TeV and the SPC measured in Pb-Pb collisions at $\sqrt{s_{NN}} = 2.76$ TeV by ALICE [21]. In Fig. 14, the comparisons for the two-harmonic SPC $\langle \cos[6(\Psi_2 - \Psi_3)] \rangle$, $\langle \cos[4(\Psi_4 - \Psi_2)] \rangle$, $\langle \cos[6(\Psi_6 - \Psi_2)] \rangle$, and $\langle \cos[6(\Psi_6 - \Psi_3)] \rangle$ are shown. With the current uncertainties, no significant deviation can be observed between the results at $\sqrt{s_{NN}} = 2.76$ TeV and

$\sqrt{s_{NN}} = 5.02$ TeV, and thus the data do not support a strong energy dependence for those two-harmonic SPC. Compared with the results in Ref. [21], the present analysis manages to extend the upper centrality limit from 50% to 60%. This extension of centrality range further indicates a decreasing correlation for $\langle \cos[4(\Psi_4 - \Psi_2)] \rangle$, $\langle \cos[6(\Psi_6 - \Psi_2)] \rangle$, and $\langle \cos[6(\Psi_6 - \Psi_3)] \rangle$ in peripheral collisions. The reason for the observed decrease in the correlation strength is discussed in Appendix A. The SPC $\langle \cos[6(\Psi_2 - \Psi_3)] \rangle$ was found to be compatible with zero within the uncertainties for all centrality intervals in the analysis at $\sqrt{s_{NN}} = 2.76$ TeV by ALICE [21]. With the increased precision of the present analysis, the correlation signal of $\langle \cos[6(\Psi_2 - \Psi_3)] \rangle$ is still compatible with zero within $n_\sigma = 2.1$. The interpretation of this absence of correlation is discussed in Sec. III C.

Similarly, Fig. 15 presents the energy dependence for three- and four-harmonic SPC. As in the case of the two-harmonic SPC, no significant energy dependence can be observed within the current uncertainties. Except for the three-harmonic SPC $\langle \cos[8\Psi_2 - 3\Psi_3 - 5\Psi_5] \rangle$, the present analysis manages to extend also the three- and four-harmonic measurements of Ref. [21] up to 60% centrality. For the two SPC $\langle \cos[8\Psi_2 - 3\Psi_3 - 5\Psi_5] \rangle$ and $\langle \cos[2\Psi_2 - 3\Psi_3 - 4\Psi_4 + 5\Psi_5] \rangle$, correlation signals are extracted in the 0–5% centrality for the first time as well. Overall, this extension adds to the available information of SPC in Pb-Pb collisions at LHC energies. Furthermore, the results at $\sqrt{s_{NN}} = 5.02$ TeV reinforce the observations from Ref. [21] of $\langle \cos[8\Psi_2 - 3\Psi_3 - 5\Psi_5] \rangle$ being compatible with zero in the whole centrality range ($n_\sigma = 0.82$ significance).

-
- [1] J.-Y. Ollitrault, Anisotropy as a signature of transverse collective flow, *Phys. Rev. D* **46**, 229 (1992).
- [2] U. Heinz and R. Snellings, Collective flow and viscosity in relativistic heavy-ion collisions, *Annu. Rev. Nucl. Part. Sci.* **63**, 123 (2013).
- [3] C. Gale, S. Jeon, and B. Schenke, Hydrodynamic modeling of heavy-ion collisions, *Int. J. Mod. Phys. A* **28**, 1340011 (2013).
- [4] M. Luzum and H. Petersen, Initial state fluctuations and final state correlations in relativistic heavy-ion collisions, *J. Phys. G* **41**, 063102 (2014).
- [5] P. Braun-Munzinger, V. Koch, T. Schäfer, and J. Stachel, Properties of hot and dense matter from relativistic heavy ion collisions, *Phys. Rep.* **621**, 76 (2016).
- [6] J. E. Bernhard, J. S. Moreland, S. A. Bass, J. Liu, and U. Heinz, Applying Bayesian parameter estimation to relativistic heavy-ion collisions: Simultaneous characterization of the initial state and quark-gluon plasma medium, *Phys. Rev. C* **94**, 024907 (2016).
- [7] C. Shen and L. Yan, Recent development of hydrodynamic modeling in heavy-ion collisions, *Nucl. Sci. Tech.* **31**, 122 (2020).
- [8] J. E. Parkkila, A. Onnerstad, and D. J. Kim, Bayesian estimation of the specific shear and bulk viscosity of the quark-gluon plasma with additional flow harmonic observables, *Phys. Rev. C* **104**, 054904 (2021).
- [9] J. E. Parkkila, A. Onnerstad, S. F. Taghavi, C. Mordasini, A. Bilandzic, M. Virta, and D. J. Kim, New constraints for QCD matter from improved Bayesian parameter estimation in heavy-ion collisions at LHC, *Phys. Lett. B* **835**, 137485 (2022).
- [10] S. Acharya *et al.* (ALICE Collaboration), The ALICE experiment: A journey through QCD, *Eur. Phys. J. C* **84**, 813 (2024).
- [11] J. E. Bernhard, P. W. Marcy, C. E. Coleman-Smith, S. Huzurbazar, R. L. Wolpert, and S. A. Bass, Quantifying properties of hot and dense QCD matter through systematic model-to-data comparison, *Phys. Rev. C* **91**, 054910 (2015).
- [12] J. Adam *et al.* (ALICE Collaboration), Correlated event-by-event fluctuations of flow harmonics in Pb-Pb collisions at $\sqrt{s_{NN}} = 2.76$ TeV, *Phys. Rev. Lett.* **117**, 182301 (2016).
- [13] S. Acharya *et al.* (ALICE Collaboration), Systematic studies of correlations between different order flow harmonics in Pb-Pb collisions at $\sqrt{s_{NN}} = 2.76$ TeV, *Phys. Rev. C* **97**, 024906 (2018).
- [14] J. E. Bernhard, J. S. Moreland, and S. A. Bass, Bayesian estimation of the specific shear and bulk viscosity of quark-gluon plasma, *Nat. Phys.* **15**, 1113 (2019).
- [15] K. Adcox *et al.* (PHENIX Collaboration), Formation of dense partonic matter in relativistic nucleus-nucleus collisions at RHIC: Experimental evaluation by the PHENIX collaboration, *Nucl. Phys. A* **757**, 184 (2005).
- [16] J. Adams *et al.* (STAR Collaboration), Experimental and theoretical challenges in the search for the quark gluon plasma: The STAR Collaboration's critical assessment of the evidence from RHIC collisions, *Nucl. Phys. A* **757**, 102 (2005).
- [17] S. Voloshin and Y. Zhang, Flow study in relativistic nuclear collisions by Fourier expansion of azimuthal particle distributions, *Z. Phys. C* **70**, 665 (1996).
- [18] S. Acharya *et al.* (ALICE Collaboration), Higher harmonic non-linear flow modes of charged hadrons in Pb-Pb collisions at $\sqrt{s_{NN}} = 5.02$ TeV, *J. High Energy Phys.* **05** (2020) 085.
- [19] S. Acharya *et al.* (ALICE Collaboration), Multiharmonic Correlations of Different Flow Amplitudes in Pb-Pb Collisions at $\sqrt{s_{NN}} = 2.76$ TeV, *Phys. Rev. Lett.* **127**, 092302 (2021).
- [20] S. Acharya *et al.* (ALICE Collaboration), Measurements of mixed harmonic cumulants in Pb-Pb collisions at $\sqrt{s_{NN}} = 5.02$ TeV, *Phys. Lett. B* **818**, 136354 (2021).
- [21] S. Acharya *et al.* (ALICE Collaboration), Symmetry plane correlations in Pb-Pb collisions at $\sqrt{s_{NN}} = 2.76$ TeV, *Eur. Phys. J. C* **83**, 576 (2023).
- [22] S. Acharya *et al.* (ALICE Collaboration), Higher-order correlations between different moments of two flow amplitudes in Pb-Pb collisions at $\sqrt{s_{NN}} = 5.02$ TeV, *Phys. Rev. C* **108**, 055203 (2023).
- [23] J. Barrette *et al.* (E877 Collaboration), Energy and charged particle flow in a 10.8A GeV/c Au + Au collisions, *Phys. Rev. C* **55**, 1420 (1997); **56**, 2336(E) (1997).
- [24] A. M. Poskanzer and S. A. Voloshin, Methods for analyzing anisotropic flow in relativistic nuclear collisions, *Phys. Rev. C* **58**, 1671 (1998).
- [25] N. Borghini, P. M. Dinh, and J.-Y. Ollitrault, A New method for measuring azimuthal distributions in nucleus-nucleus collisions, *Phys. Rev. C* **63**, 054906 (2001).
- [26] N. Borghini, P. M. Dinh, and J.-Y. Ollitrault, Flow analysis from multiparticle azimuthal correlations, *Phys. Rev. C* **64**, 054901 (2001).

- [27] A. Bilandzic, R. Snellings, and S. Voloshin, Flow analysis with cumulants: Direct calculations, *Phys. Rev. C* **83**, 044913 (2011).
- [28] R. S. Bhalerao, M. Luzum, and J.-Y. Ollitrault, Determining initial-state fluctuations from flow measurements in heavy-ion collisions, *Phys. Rev. C* **84**, 034910 (2011).
- [29] A. Bilandzic, C. H. Christensen, K. Gulbrandsen, A. Hansen, and Y. Zhou, Generic framework for anisotropic flow analyses with multiparticle azimuthal correlations, *Phys. Rev. C* **89**, 064904 (2014).
- [30] A. Bilandzic, M. Lesch, and S. F. Taghavi, New estimator for symmetry plane correlations in anisotropic flow analyses, *Phys. Rev. C* **102**, 024910 (2020).
- [31] C. Adler *et al.* (STAR Collaboration), Identified particle elliptic flow in Au + Au collisions at $\sqrt{s_{NN}} = 130$ GeV, *Phys. Rev. Lett.* **87**, 182301 (2001).
- [32] C. Adler *et al.* (STAR Collaboration), Elliptic flow from two and four particle correlations in Au+Au collisions at $\sqrt{s_{NN}} = 130$ GeV, *Phys. Rev. C* **66**, 034904 (2002).
- [33] J. Adams *et al.* (STAR Collaboration), Azimuthal anisotropy at RHIC: The first and fourth harmonics, *Phys. Rev. Lett.* **92**, 062301 (2004); **127**, 069901(E) (2021).
- [34] K. Aamodt *et al.* (ALICE Collaboration), Higher harmonic anisotropic flow measurements of charged particles in Pb–Pb collisions at $\sqrt{s_{NN}} = 2.76$ TeV, *Phys. Rev. Lett.* **107**, 032301 (2011).
- [35] M. Aaboud *et al.* (ATLAS Collaboration), Measurement of the azimuthal anisotropy of charged particles produced in $\sqrt{s_{NN}} = 5.02$ TeV Pb+Pb collisions with the ATLAS detector, *Eur. Phys. J. C* **78**, 997 (2018).
- [36] C. Mordasini, A. Bilandzic, D. Karakoç, and S. F. Taghavi, Higher order Symmetric Cumulants, *Phys. Rev. C* **102**, 024907 (2020).
- [37] Z. Moravcova, K. Gulbrandsen, and Y. Zhou, Generic algorithm for multiparticle cumulants of azimuthal correlations in high energy nucleus collisions, *Phys. Rev. C* **103**, 024913 (2021).
- [38] A. Bilandzic, M. Lesch, C. Mordasini, and S. F. Taghavi, Multivariate cumulants in flow analyses: The next generation, *Phys. Rev. C* **105**, 024912 (2022).
- [39] G. Aad *et al.* (ATLAS Collaboration), Measurement of event-plane correlations in $\sqrt{s_{NN}} = 2.76$ TeV lead-lead collisions with the ATLAS detector, *Phys. Rev. C* **90**, 024905 (2014).
- [40] S. Acharya *et al.* (ALICE Collaboration), Linear and non-linear flow modes in Pb–Pb collisions at $\sqrt{s_{NN}} = 2.76$ TeV, *Phys. Lett. B* **773**, 68 (2017).
- [41] K. Aamodt *et al.* (ALICE Collaboration), The ALICE experiment at the CERN LHC, *J. Instrum.* **3**, S08002 (2008).
- [42] B. Abelev *et al.* (ALICE Collaboration), Performance of the ALICE experiment at the CERN LHC, *Int. J. Mod. Phys. A* **29**, 1430044 (2014).
- [43] E. Abbas *et al.* (ALICE Collaboration), Performance of the ALICE VZERO system, *J. Instrum.* **8**, P10016 (2013).
- [44] J. Alme *et al.*, The ALICE TPC, a large 3-dimensional tracking device with fast readout for ultra-high multiplicity events, *Nucl. Instrum. Methods A* **622**, 316 (2010).
- [45] B. Abelev *et al.* (ALICE Collaboration), Technical design report for the upgrade of the ALICE inner tracking system, *J. Phys. G* **41**, 087002 (2014).
- [46] K. Aamodt *et al.* (ALICE Collaboration), Alignment of the ALICE inner tracking system with cosmic-ray tracks, *J. Instrum.* **5**, P03003 (2010).
- [47] M. Arslanodk, E. Hellbär, M. Ivanov, R. H. Münzer, and J. Wiechula, Track reconstruction in a high-density environment with ALICE, *Particles* **5**, 84 (2022).
- [48] A. Akindinov *et al.*, Performance of the ALICE time-of-flight detector at the LHC, *Eur. Phys. J. Plus* **128**, 44 (2013).
- [49] S. Acharya *et al.* (ALICE Collaboration), Transverse momentum spectra and nuclear modification factors of charged particles in pp, p-Pb and Pb-Pb collisions at the LHC, *J. High Energy Phys.* **11** (2018) 013.
- [50] S. Acharya *et al.* (ALICE Collaboration), Anisotropic flow and flow fluctuations of identified hadrons in Pb–Pb collisions at $\sqrt{s_{NN}} = 5.02$ TeV, *J. High Energy Phys.* **05** (2023) 243.
- [51] M. Gyulassy and X.-N. Wang, HIJING 1.0: A Monte Carlo program for parton and particle production in high-energy hadronic and nuclear collisions, *Comput. Phys. Commun.* **83**, 307 (1994).
- [52] R. Brun, F. Bruyant, F. Carminati, S. Giani, M. Maire, A. McPherson, G. Patrick, and L. Urban, GEANT: Detector Description and Simulation Tool, Oct. 1994, Long Writeup W5013 (unpublished), <http://cds.cern.ch/record/1082634>
- [53] R. Barlow, Systematic errors: Facts and fictions, in *Conference on Advanced Statistical Techniques in Particle Physics* (Durham University, Durham, UK, 2002), pp. 134–144.
- [54] H. Mehrabpour and S. F. Taghavi, Non-Bessel–Gaussianity and flow harmonic fine-splitting, *Eur. Phys. J. C* **79**, 88 (2019).
- [55] L. Yan, J.-Y. Ollitrault, and A. M. Poskanzer, Eccentricity distributions in nucleus-nucleus collisions, *Phys. Rev. C* **90**, 024903 (2014).
- [56] D. Teaney and L. Yan, Triangularity and dipole asymmetry in heavy ion collisions, *Phys. Rev. C* **83**, 064904 (2011).
- [57] D. Teaney and L. Yan, Nonlinearities in the harmonic spectrum of heavy ion collisions with ideal and viscous hydrodynamics, *Phys. Rev. C* **86**, 044908 (2012).
- [58] D. Teaney and L. Yan, Event-plane correlations and hydrodynamic simulations of heavy ion collisions, *Phys. Rev. C* **90**, 024902 (2014).
- [59] H. Niemi, K. J. Eskola, and R. Paatelainen, Event-by-event fluctuations in a perturbative QCD+saturation+hydrodynamics model: Determining QCD matter shear viscosity in ultrarelativistic heavy-ion collisions, *Phys. Rev. C* **93**, 024907 (2016).
- [60] H. Hirvonen, K. J. Eskola, and H. Niemi, Flow correlations from a hydrodynamics model with dynamical freeze-out and initial conditions based on perturbative QCD and saturation, *Phys. Rev. C* **106**, 044913 (2022).
- [61] R. Paatelainen, K. J. Eskola, H. Holopainen, and K. Tuominen, Multiplicities and p_T spectra in ultrarelativistic heavy ion collisions from a next-to-leading order improved perturbative QCD + saturation + hydrodynamics model, *Phys. Rev. C* **87**, 044904 (2013).
- [62] R. Paatelainen, K. J. Eskola, H. Niemi, and K. Tuominen, Fluid dynamics with saturated minijet initial conditions in ultrarelativistic heavy-ion collisions, *Phys. Lett. B* **731**, 126 (2014).
- [63] S. A. Bass *et al.*, Microscopic models for ultrarelativistic heavy ion collisions, *Prog. Part. Nucl. Phys.* **41**, 255 (1998).
- [64] M. Bleicher *et al.*, Relativistic hadron hadron collisions in the ultrarelativistic quantum molecular dynamics model, *J. Phys. G* **25**, 1859 (1999).
- [65] H. Song and U. W. Heinz, Causal viscous hydrodynamics in 2 + 1 dimensions for relativistic heavy-ion collisions, *Phys. Rev. C* **77**, 064901 (2008).

- [66] C. Shen, Z. Qiu, H. Song, J. Bernhard, S. Bass, and U. Heinz, The iEBE-VISHNU code package for relativistic heavy-ion collisions, *Comput. Phys. Commun.* **199**, 61 (2016).
- [67] J. S. Moreland, J. E. Bernhard, and S. A. Bass, Alternative ansatz to wounded nucleon and binary collision scaling in high-energy nuclear collisions, *Phys. Rev. C* **92**, 011901(R) (2015).
- [68] F. G. Gardim, F. Grassi, M. Luzum, and J.-Y. Ollitrault, Mapping the hydrodynamic response to the initial geometry in heavy-ion collisions, *Phys. Rev. C* **85**, 024908 (2012).
- [69] S. F. Taghavi, A Fourier-cumulant analysis for multiharmonic flow fluctuation: by employing a multidimensional generating function approach, *Eur. Phys. J. C* **81**, 652 (2021).
- [70] H. Niemi, K. J. Eskola, R. Paatelainen, and K. Tuominen, Predictions for 5.023 TeV Pb + Pb collisions at the CERN Large Hadron Collider, *Phys. Rev. C* **93**, 014912 (2016).
- [71] J. Noronha-Hostler, M. Luzum, and J.-Y. Ollitrault, Hydrodynamic predictions for 5.02 TeV Pb-Pb collisions, *Phys. Rev. C* **93**, 034912 (2016).

S. Acharya¹²⁷, A. Agarwal¹³⁵, G. Aglieri Rinella³², L. Aglietta²⁴, M. Agnello²⁹, N. Agrawal²⁵, Z. Ahammed¹³⁵, S. Ahmad¹⁵, S. U. Ahn⁷¹, I. Ahuja³⁷, A. Akindinov¹⁴¹, V. Akishina³⁸, M. Al-Turany⁹⁷, D. Aleksandrov¹⁴¹, B. Alessandro⁵⁶, H. M. Alfanda⁶, R. Alfaro Molina⁶⁷, B. Ali¹⁵, A. Alici²⁵, N. Alizadehvandchali¹¹⁶, A. Alkin¹⁰⁴, J. Alme²⁰, G. Alocco^{24,52}, T. Alt⁶⁴, A. R. Altamura⁵⁰, I. Altsybeev⁹⁵, J. R. Alvarado⁴⁴, M. N. Anaam⁶, C. Andrei⁴⁵, N. Androun¹¹⁵, A. Andronic¹²⁶, E. Andronov¹⁴¹, V. Anguelov⁹⁴, F. Antinori⁵⁴, P. Antonioli⁵¹, N. Apadula⁷⁴, L. Aphecetche¹⁰³, H. Appelshäuser⁶⁴, C. Arata⁷³, S. Arcelli²⁵, R. Arnaldi⁵⁶, J. G. M. C. A. Arneiro¹¹⁰, I. C. Arsene¹⁹, M. Arslanodok¹³⁸, A. Augustinus³², R. Averbeck⁹⁷, D. Averyanov¹⁴¹, M. D. Azmi¹⁵, H. Baba¹²⁴, A. Badalà⁵³, J. Bae¹⁰⁴, Y. W. Baek⁴⁰, X. Bai¹²⁰, R. Bailhache⁶⁴, Y. Bailung⁴⁸, R. Bala⁹¹, A. Balbino²⁹, A. Baldisseri¹³⁰, B. Balis², D. Banerjee⁴, Z. Banoo⁹¹, V. Barbasova³⁷, F. Barile³¹, L. Barioglio⁵⁶, M. Barlou⁷⁸, B. Barman⁴¹, G. G. Barnaföldi⁴⁶, L. S. Barnby¹¹⁵, E. Barreau¹⁰³, V. Barret¹²⁷, L. Barreto¹¹⁰, C. Bartels¹¹⁹, K. Barth³², E. Bartsch⁶⁴, N. Bastid¹²⁷, S. Basu⁷⁵, G. Batigne¹⁰³, D. Battistini⁹⁵, B. Batyunya¹⁴², D. Bauri⁴⁷, J. L. Bazo Alba¹⁰¹, I. G. Bearden⁸³, C. Beattie¹³⁸, P. Becht⁹⁷, D. Behera⁴⁸, I. Belikov¹²⁹, A. D. C. Bell Hechavarria¹²⁶, F. Bellini²⁵, R. Bellwied¹¹⁶, S. Belokurova¹⁴¹, L. G. E. Beltran¹⁰⁹, Y. A. V. Beltran⁴⁴, G. Bencedi⁴⁶, A. Bensaoula¹¹⁶, S. Beole²⁴, Y. Berdnikov¹⁴¹, A. Berdnikova⁹⁴, L. Bergmann⁹⁴, M. G. Besoiu⁶³, L. Betev³², P. P. Bhaduri¹³⁵, A. Bhasin⁹¹, B. Bhattacharjee⁴¹, L. Bianchi²⁴, J. Bielčik³⁵, J. Bielčíková⁸⁶, A. P. Bigot¹²⁹, A. Bilandzic⁹⁵, G. Biro⁴⁶, S. Biswas⁴, N. Bize¹⁰³, J. T. Blair¹⁰⁸, D. Blau¹⁴¹, M. B. Blidaru⁹⁷, N. Bluhme³⁸, C. Blume⁶⁴, G. Boca^{21,55}, F. Bock⁸⁷, T. Bodova²⁰, J. Bok¹⁶, L. Boldizsár⁴⁶, M. Bombara³⁷, P. M. Bond³², G. Bonomi^{134,55}, H. Borel¹³⁰, A. Borissov¹⁴¹, A. G. Borquez Carcamo⁹⁴, E. Botta²⁴, Y. E. M. Bouziani⁶⁴, L. Bratrud⁶⁴, P. Braun-Munzinger⁹⁷, M. Bregant¹¹⁰, M. Broz³⁵, G. E. Bruno^{96,31}, V. D. Buchakchiev³⁶, M. D. Buckland⁸⁵, D. Budnikov¹⁴¹, H. Buesching⁶⁴, S. Bufalino²⁹, P. Buhler¹⁰², N. Burmasov¹⁴¹, Z. Buthelezi^{68,123}, A. Bylinkin²⁰, S. A. Bysiak¹⁰⁷, J. C. Cabanillas Noris¹⁰⁹, M. F. T. Cabrera¹¹⁶, M. Cai⁶, H. Caines¹³⁸, A. Caliva²⁸, E. Calvo Villar¹⁰¹, J. M. M. Camacho¹⁰⁹, P. Camerini²³, F. D. M. Canedo¹¹⁰, S. L. Cantway¹³⁸, M. Carabas¹¹³, A. A. Carballo³², F. Carnesecchi³², R. Caron¹²⁸, L. A. D. Carvalho¹¹⁰, J. Castillo Castellanos¹³⁰, M. Castoldi³², F. Catalano³², S. Cattaruzzi²³, C. Ceballos Sanchez¹⁴², R. Cerri²⁴, I. Chakaberia⁷⁴, P. Chakraborty¹³⁶, S. Chandra¹³⁵, S. Chapeland³², M. Chartier¹¹⁹, S. Chattopadhyay¹³⁵, S. Chattopadhyay¹³⁵, S. Chattopadhyay⁹⁹, M. Chen³⁹, T. Cheng⁶, C. Cheshkov¹²⁸, V. Chibante Barroso³², D. D. Chinellato¹⁰², E. S. Chizzali^{95,a}, J. Cho⁵⁸, S. Cho⁵⁸, P. Chochula³², Z. A. Chochulska¹³⁶, D. Choudhury⁴¹, P. Christakoglou⁸⁴, C. H. Christensen⁸³, P. Christiansen⁷⁵, T. Chujo¹²⁵, M. Ciacco²⁹, C. Cicalo⁵², M. R. Ciupek⁹⁷, G. Clai^{51,b}, F. Colamaria⁵⁰, J. S. Colburn¹⁰⁰, D. Colella³¹, A. Colelli³¹, M. Colocci²⁵, M. Concas³², G. Conesa Balbastre⁷³, Z. Conesa del Valle¹³¹, G. Contin²³, J. G. Contreras³⁵, M. L. Coquet¹⁰³, P. Cortese^{133,56}, M. R. Cosentino¹¹², F. Costa³², S. Costanza^{21,55}, C. Cot¹³¹, P. Crochet¹²⁷, R. Cruz-Torres⁷⁴, M. M. Czarnynoga¹³⁶, A. Dainese⁵⁴, G. Dange³⁸, M. C. Danisch⁹⁴, A. Danu⁶³, P. Das⁸⁰, S. Das⁴, A. R. Dash¹²⁶, S. Dash⁴⁷, A. De Caro²⁸, G. de Cataldo⁵⁰, J. de Cuveland³⁸, A. De Falco²², D. De Gruttola²⁸, N. De Marco⁵⁶, C. De Martin²³, S. De Pasquale²⁸, R. Deb¹³⁴, R. Del Grande⁹⁵, L. Dello Stritto³², W. Deng⁶, K. C. Devereaux¹⁸, P. Dhankher¹⁸, D. Di Bari³¹, A. Di Mauro³², B. Di Ruzza¹³², B. Diab¹³⁰, R. A. Diaz^{142,7}, T. Dietel¹¹⁴, Y. Ding⁶, J. Ditzel⁶⁴, R. Divià³², Ø. Djuvsland²⁰, U. Dmitrieva¹⁴¹, A. Dobrin⁶³, B. Dönigus⁶⁴, J. M. Dubinski¹³⁶, A. Dubla⁹⁷, P. Dupieux¹²⁷, N. Dzalaiova¹³, T. M. Eder¹²⁶, R. J. Ehlers⁷⁴, F. Eisenhut⁶⁴, R. Ejima⁹², D. Elia⁵⁰, B. Erazmus¹⁰³, F. Ercolessi²⁵, B. Espagnon¹³¹, G. Eulisse³², D. Evans¹⁰⁰, S. Evdokimov¹⁴¹, L. Fabbietti⁹⁵, M. Faggin²³, J. Faivre⁷³, F. Fan⁶, W. Fan⁷⁴, A. Fantoni⁴⁹, M. Fasel⁸⁷, A. Feliciello⁵⁶, G. Feofilov¹⁴¹, A. Fernández Téllez⁴⁴, L. Ferrandi¹¹⁰, M. B. Ferrer³², A. Ferrero¹³⁰, C. Ferrero^{56,c}, A. Ferretti²⁴, V. J. G. Feuillard⁹⁴, V. Filova³⁵, D. Finogeev¹⁴¹, F. M. Fionda⁵², E. Flatland³², F. Flor^{138,116}, A. N. Flores¹⁰⁸, S. Foertsch⁶⁸, I. Fokin⁹⁴, S. Fokin¹⁴¹, U. Follo^{56,c}, E. Fragiaco⁵⁷, E. Frajna⁴⁶, U. Fuchs³², N. Funicello²⁸, C. Furget⁷³, A. Furs¹⁴¹, T. Fusayasu⁹⁸, J. J. Gaardhøje⁸³, M. Gagliardi²⁴, A. M. Gago¹⁰¹, T. Gahlaut⁴⁷, C. D. Galvan¹⁰⁹, D. R. Gangadharan¹¹⁶, P. Ganoti⁷⁸, C. Garabatos⁹⁷, J. M. Garcia⁴⁴, T. García Chávez⁴⁴, E. Garcia-Solis⁹, C. Gargiulo³², P. Gasik⁹⁷, H. M. Gaur³⁸, A. Gautam¹¹⁸, M. B. Gay Ducati⁶⁶, M. Germain¹⁰³, R. A. Gernhaeuser⁹⁵, C. Ghosh¹³⁵, M. Giacalone⁵¹, G. Gioachin²⁹, S. K. Giri¹³⁵, P. Giubellino^{97,56}, P. Giubilato²⁷, A. M. C. Glaenger¹³⁰

- P. Glässel ⁹⁴, E. Glimos ¹²², D. J. Q. Goh ⁷⁶, V. Gonzalez ¹³⁷, P. Gordeev ¹⁴¹, M. Gorgon ², K. Goswami ⁴⁸, S. Gotovac ³³, V. Grabski ⁶⁷, L. K. Graczykowski ¹³⁶, E. Grecka ⁸⁶, A. Grelli ⁵⁹, C. Grigoras ³², V. Grigoriev ¹⁴¹, S. Grigoryan ^{142,1}, F. Grosa ³², J. F. Grosse-Oetringhaus ³², R. Grosso ⁹⁷, D. Grund ³⁵, N. A. Grunwald ⁹⁴, G. G. Guardiano ¹¹¹, R. Guernane ⁷³, M. Guilbaud ¹⁰³, K. Gulbrandsen ⁸³, J. J. W. K. Gumprecht ¹⁰², T. Gündem ⁶⁴, T. Gunji ¹²⁴, W. Guo ⁶, A. Gupta ⁹¹, R. Gupta ⁹¹, R. Gupta ⁴⁸, K. Gwizdzziel ¹³⁶, L. Gyulai ⁴⁶, C. Hadjidakis ¹³¹, F. U. Haider ⁹¹, S. Haidlova ³⁵, M. Haldar ⁴, H. Hamagaki ⁷⁶, Y. Han ¹³⁹, B. G. Hanley ¹³⁷, R. Hannigan ¹⁰⁸, J. Hansen ⁷⁵, M. R. Haque ⁹⁷, J. W. Harris ¹³⁸, A. Harton ⁹, M. V. Hartung ⁶⁴, H. Hassan ¹¹⁷, D. Hatzifotiadiou ⁵¹, P. Hauer ⁴², L. B. Havener ¹³⁸, E. Hellbär ³², H. Helstrup ³⁴, M. Hemmer ⁶⁴, T. Herman ³⁵, S. G. Hernandez ¹¹⁶, G. Herrera Corral ⁸, S. Herrmann ¹²⁸, K. F. Hetland ³⁴, B. Heybeck ⁶⁴, H. Hillemanns ³², B. Hippolyte ¹²⁹, I. P. M. Hobus ⁸⁴, F. W. Hoffmann ⁷⁰, B. Hofman ⁵⁹, G. H. Hong ¹³⁹, M. Horst ⁹⁵, A. Horzyk ², Y. Hou ⁶, P. Hristov ³², P. Huhn ⁶⁴, L. M. Huhta ¹¹⁷, T. J. Humanic ⁸⁸, A. Hutson ¹¹⁶, D. Hutter ³⁸, M. C. Hwang ¹⁸, R. Ilkaev ¹⁴¹, M. Inaba ¹²⁵, G. M. Innocenti ³², M. Ippolitov ¹⁴¹, A. Isakov ⁸⁴, T. Isidori ¹¹⁸, M. S. Islam ⁹⁹, S. Iurchenko ¹⁴¹, M. Ivanov ⁹⁷, M. Ivanov ¹³, V. Ivanov ¹⁴¹, K. E. Iversen ⁷⁵, M. Jablonski ², B. Jacak ^{18,74}, N. Jacazio ²⁵, P. M. Jacobs ⁷⁴, S. Jadlovská ¹⁰⁶, J. Jadlovsky ¹⁰⁶, S. Jaelani ⁸², C. Jahnke ¹¹⁰, M. J. Jakubowska ¹³⁶, M. A. Janik ¹³⁶, T. Janson ⁷⁰, S. Ji ¹⁶, S. Jia ¹⁰, T. Jiang ¹⁰, A. A. P. Jimenez ⁶⁵, F. Jonas ⁷⁴, D. M. Jones ¹¹⁹, J. M. Jowett ^{32,97}, J. Jung ⁶⁴, M. Jung ⁶⁴, A. Junique ³², A. Jusko ¹⁰⁰, J. Kaewjai ¹⁰⁵, P. Kalinak ⁶⁰, A. Kalweit ³², A. Karasu Uysal ^{72,d}, D. Karatovic ⁸⁹, N. Karatzenis ¹⁰⁰, O. Karavichev ¹⁴¹, T. Karavicheva ¹⁴¹, E. Karpechev ¹⁴¹, M. J. Karwowska ^{32,136}, U. Kebschull ⁷⁰, R. Keidel ¹⁴⁰, M. Keil ³², B. Ketzer ⁴², J. Keul ⁶⁴, S. S. Khade ⁴⁸, A. M. Khan ¹²⁰, S. Khan ¹⁵, A. Khanzadeev ¹⁴¹, Y. Kharlov ¹⁴¹, A. Khatun ¹¹⁸, A. Khuntia ³⁵, Z. Khuranova ⁶⁴, B. Kileng ³⁴, B. Kim ¹⁰⁴, C. Kim ¹⁶, D. J. Kim ¹¹⁷, E. J. Kim ⁶⁹, J. Kim ¹³⁹, J. Kim ⁵⁸, J. Kim ^{32,69}, M. Kim ¹⁸, S. Kim ¹⁷, T. Kim ¹³⁹, K. Kimura ⁹², A. Kirkova ³⁶, S. Kirsch ⁶⁴, I. Kisel ³⁸, S. Kiselev ¹⁴¹, A. Kisiel ¹³⁶, J. P. Kitowski ², J. L. Klay ⁵, J. Klein ³², S. Klein ⁷⁴, C. Klein-Bösing ¹²⁶, M. Kleiner ⁶⁴, T. Klemenz ⁹⁵, A. Kluge ³², C. Kobdaj ¹⁰⁵, R. Kohara ¹²⁴, T. Kollegger ⁹⁷, A. Kondratyev ¹⁴², N. Kondratyeva ¹⁴¹, J. König ⁶⁴, S. A. Konigstorfer ⁹⁵, P. J. Konopka ³², G. Kornakov ¹³⁶, M. Korwieser ⁹⁵, S. D. Koryciak ², C. Koster ⁸⁴, A. Kotliarov ⁸⁶, N. Kovacic ⁸⁹, V. Kovalenko ¹⁴¹, M. Kowalski ¹⁰⁷, V. Kozuharov ³⁶, G. Kozlov ³⁸, I. Králik ⁶⁰, A. Kravčáková ³⁷, L. Krcal ^{32,38}, M. Krivda ^{100,60}, F. Krizek ⁸⁶, K. Krizkova Gajdosova ³², C. Krug ⁶⁶, M. Krüger ⁶⁴, D. M. Krupova ³⁵, E. Kryshen ¹⁴¹, V. Kučera ⁵⁸, C. Kuhn ¹²⁹, P. G. Kujfer ⁸⁴, T. Kumaoka ¹²⁵, D. Kumar ¹³⁵, L. Kumar ⁹⁰, N. Kumar ⁹⁰, S. Kumar ⁵⁰, S. Kundu ³², P. Kurashvili ⁷⁹, A. Kurepin ¹⁴¹, A. B. Kurepin ¹⁴¹, A. Kuryakin ¹⁴¹, S. Kushpil ⁸⁶, V. Kuskov ¹⁴¹, M. Kutyla ¹³⁶, A. Kuznetsov ¹⁴², M. J. Kweon ⁵⁸, Y. Kwon ¹³⁹, S. L. La Pointe ³⁸, P. La Rocca ²⁶, A. Lakrathok ¹⁰⁵, M. Lamanna ³², A. R. Landou ⁷³, R. Langoy ¹²¹, P. Larionov ³², E. Laudi ³², L. Lautner ^{32,95}, R. A. N. Laveaga ¹⁰⁹, R. Lavicka ¹⁰², R. Lea ^{134,55}, H. Lee ¹⁰⁴, I. Legrand ⁴⁵, G. Legras ¹²⁶, J. Lehrbach ³⁸, A. M. Lejeune ³⁵, T. M. Lelek ², R. C. Lemmon ^{85,e}, I. León Monzón ¹⁰⁹, M. M. Lesch ⁹⁵, E. D. Lesser ¹⁸, P. Lévai ⁴⁶, M. Li ⁶, P. Li ¹⁰, X. Li ¹⁰, B. E. Liang-Gilman ¹⁸, J. Lien ¹²¹, R. Lietava ¹⁰⁰, I. Likmeta ¹¹⁶, B. Lim ²⁴, S. H. Lim ¹⁶, V. Lindenstruth ³⁸, A. Lindner ⁴⁵, C. Lippmann ⁹⁷, D. H. Liu ⁶, J. Liu ¹¹⁹, G. S. S. Liveraro ¹¹¹, I. M. Lofnes ²⁰, C. Loizides ⁸⁷, S. Lokos ¹⁰⁷, J. Lömker ⁵⁹, X. Lopez ¹²⁷, E. López Torres ⁷, C. Lotteau ¹²⁸, P. Lu ^{97,120}, Z. Lu ¹⁰, F. V. Lugo ⁶⁷, J. R. Luhder ¹²⁶, M. Lunardon ²⁷, G. Luparello ⁵⁷, Y. G. Ma ³⁹, M. Mager ³², A. Maire ¹²⁹, E. M. Majerz ², M. V. Makariev ³⁶, M. Malaev ¹⁴¹, G. Malfattore ²⁵, N. M. Malik ⁹¹, S. K. Malik ⁹¹, L. Malinina ^{142,e,f}, D. Mallick ¹³¹, N. Mallick ⁴⁸, G. Mandaglio ^{30,53}, S. K. Mandal ⁷⁹, A. Manea ⁶³, V. Manko ¹⁴¹, F. Manso ¹²⁷, V. Manzari ⁵⁰, Y. Mao ⁶, R. W. Marcjan ², G. V. Margagliotti ²³, A. Margotti ⁵¹, A. Marín ⁹⁷, C. Markert ¹⁰⁸, C. F. B. Marquez ³¹, P. Martinengo ³², M. I. Martínez ⁴⁴, G. Martínez García ¹⁰³, M. P. P. Martins ¹¹⁰, S. Masciocchi ⁹⁷, M. Masera ²⁴, A. Masoni ⁵², L. Massacrier ¹³¹, O. Massen ⁵⁹, A. Mastroserio ^{132,50}, O. Matonoha ⁷⁵, S. Mattiazzo ²⁷, A. Matyja ¹⁰⁷, F. Mazzaschi ^{32,24}, M. Mazzilli ¹¹⁶, Y. Melikyan ⁴³, M. Melo ¹¹⁰, A. Menchaca-Rocha ⁶⁷, J. E. M. Mendez ⁶⁵, E. Meninno ¹⁰², A. S. Menon ¹¹⁶, M. W. Menzel ^{32,94}, M. Meres ¹³, Y. Miake ¹²⁵, L. Micheletti ³², D. L. Mihaylov ⁹⁵, K. Mikhaylov ^{142,141}, N. Minafra ¹¹⁸, D. Miśkowiec ⁹⁷, A. Modak ¹³⁴, B. Mohanty ⁸⁰, M. Mohisin Khan ^{15,g}, M. A. Molander ⁴³, S. Monira ¹³⁶, C. Mordasini ¹¹⁷, D. A. Moreira De Godoy ¹²⁶, I. Morozov ¹⁴¹, A. Morsch ³², T. Mrnjavac ³², V. Muccifora ⁴⁹, S. Muhuri ¹³⁵, J. D. Mulligan ⁷⁴, A. Mulliri ²², M. G. Munhoz ¹¹⁰, R. H. Munzer ⁶⁴, H. Murakami ¹²⁴, S. Murray ¹¹⁴, L. Musa ³², J. Musinsky ⁶⁰, J. W. Myrcha ¹³⁶, B. Naik ¹²³, A. I. Nambrath ¹⁸, B. K. Nandi ⁴⁷, R. Nania ⁵¹, E. Nappi ⁵⁰, A. F. Nassirpour ¹⁷, A. Nath ⁹⁴, S. Nath ¹³⁵, C. Nattrass ¹²², M. N. Naydenov ³⁶, A. Neagu ¹⁹, A. Negru ¹¹³, E. Nekrasova ¹⁴¹, L. Nellen ⁶⁵, R. Nepeivoda ⁷⁵, S. Nese ¹⁹, N. Nicassio ⁵⁰, B. S. Nielsen ⁸³, E. G. Nielsen ⁸³, S. Nikolaev ¹⁴¹, S. Nikulin ¹⁴¹, V. Nikulin ¹⁴¹, F. Noferini ⁵¹, S. Noh ¹², P. Nomokonov ¹⁴², J. Norman ¹¹⁹, N. Novitzky ⁸⁷, P. Nowakowski ¹³⁶, A. Nyanin ¹⁴¹, J. Nystrand ²⁰, S. Oh ¹⁷, A. Ohlson ⁷⁵, V. A. Okorokov ¹⁴¹, J. Oleniacz ¹³⁶, A. Onnerstad ¹¹⁷, C. Oppedisano ⁵⁶, A. Ortiz Velasquez ⁶⁵, J. Otwinowski ¹⁰⁷, M. Oya ⁹², K. Oyama ⁷⁶, Y. Pachmayer ⁹⁴, S. Padhan ⁴⁷, D. Pagano ^{134,55}, G. Paic ⁶⁵, S. Paisano-Guzmán ⁴⁴, A. Palasciano ⁵⁰, I. Panasenکو ⁷⁵, S. Panebianco ¹³⁰, C. Pantouvakis ²⁷, H. Park ¹²⁵, H. Park ¹⁰⁴, J. Park ¹²⁵, J. E. Parkkila ³², Y. Patley ⁴⁷, R. N. Patra ⁵⁰, B. Paul ¹³⁵, H. Pei ⁶, T. Peitzmann ⁵⁹, X. Peng ¹¹, M. Pennisi ²⁴, S. Perciballi ²⁴, D. Peresunko ¹⁴¹, G. M. Perez ⁷, Y. Pestov ¹⁴¹, M. T. Petersen ⁸³, V. Petrov ¹⁴¹, M. Petrovici ⁴⁵, S. Piano ⁵⁷, M. Pikna ¹³, P. Pillot ¹⁰³, O. Pinazza ^{51,32}, L. Pinsky ¹¹⁶, C. Pinto ⁹⁵, S. Pisano ⁴⁹, M. Płoskoń ⁷⁴, M. Planinic ⁸⁹, F. Pliquett ⁶⁴, D. K. Plociennik ², M. G. Poghosyan ⁸⁷, B. Polichtchouk ¹⁴¹, S. Politano ²⁹

N. Poljak⁸⁹, A. Pop⁴⁵, S. Porteboeuf-Houssais¹²⁷, V. Pozdniakov^{142,e}, I. Y. Pozos⁴⁴, K. K. Pradhan⁴⁸, S. K. Prasad⁴, S. Prasad⁴⁸, R. Preghenella⁵¹, F. Prino⁵⁶, C. A. Pruneau¹³⁷, I. Pshenichnov¹⁴¹, M. Puccio³², S. Pucillo²⁴, S. Qiu⁸⁴, L. Quaglia²⁴, A. M. K. Radhakrishnan⁴⁸, S. Ragoni¹⁴, A. Rai¹³⁸, A. Rakotozafindrabe¹³⁰, L. Ramello^{133,56}, F. Rami¹²⁹, C. O. Ramírez-Álvarez⁴⁴, M. Rasa²⁶, S. S. Räsänen⁴³, R. Rath⁵¹, M. P. Rauch²⁰, I. Ravasenga³², K. F. Read^{87,122}, C. Reckziegel¹¹², A. R. Redelbach³⁸, K. Redlich^{79,h}, C. A. Reetz⁹⁷, H. D. Regules-Medel⁴⁴, A. Rehman²⁰, F. Reidt³², H. A. Reme-Ness³⁴, K. Reygers⁹⁴, A. Riabov¹⁴¹, V. Riabov¹⁴¹, R. Ricci²⁸, M. Richter²⁰, A. A. Riedel⁹⁵, W. Riegler³², A. G. Riffero²⁴, M. Rignanese²⁷, C. Ripoli²⁸, C. Ristea⁶³, M. V. Rodriguez³², M. Rodríguez Cahuantzi⁴⁴, S. A. Rodríguez Ramírez⁴⁴, K. Røed¹⁹, R. Rogalev¹⁴¹, E. Rogochaya¹⁴², T. S. Rogoschinski⁶⁴, D. Rohr³², D. Röhrich²⁰, S. Rojas Torres³⁵, P. S. Rokita¹³⁶, G. Romanenko²⁵, F. Ronchetti³², E. D. Rosas⁶⁵, K. Roslon¹³⁶, A. Rossi⁵⁴, A. Roy⁴⁸, S. Roy⁴⁷, N. Rubini^{51,25}, J. A. Rudolph⁸⁴, D. Ruggiano¹³⁶, R. Rui²³, P. G. Russek², R. Russo⁸⁴, A. Rustamov⁸¹, E. Ryabinkin¹⁴¹, Y. Ryabov¹⁴¹, A. Rybicki¹⁰⁷, J. Ryu¹⁶, W. Rzeska¹³⁶, B. Sabiu⁵¹, S. Sadovsky¹⁴¹, J. Saetre²⁰, K. Šafařík³⁵, S. Saha⁸⁰, B. Sahoo⁴⁸, R. Sahoo⁴⁸, S. Sahoo⁶¹, D. Sahu⁴⁸, P. K. Sahu⁶¹, J. Saini¹³⁵, K. Sajdakova³⁷, S. Sakai¹²⁵, M. P. Salvan⁹⁷, S. Sambyal⁹¹, D. Samitz¹⁰², I. Sanna^{32,95}, T. B. Saramela¹¹⁰, D. Sarkar⁸³, P. Sarma⁴¹, V. Sarritzu²², V. M. Sarti⁹⁵, M. H. P. Sas³², S. Sawan⁸⁰, E. Scapparone⁵¹, J. Schambach⁸⁷, H. S. Scheid⁶⁴, C. Schiaua⁴⁵, R. Schicker⁹⁴, F. Schlepfer⁹⁴, A. Schmah⁹⁷, C. Schmidt⁹⁷, H. R. Schmidt⁹³, M. O. Schmidt³², M. Schmidt⁹³, N. V. Schmidt⁸⁷, A. R. Schmier¹²², R. Schotter^{102,129}, A. Schröter³⁸, J. Schukraft³², K. Schweda⁹⁷, G. Scioli²⁵, E. Scomparin⁵⁶, J. E. Seger¹⁴, Y. Sekiguchi¹²⁴, D. Sekihata¹²⁴, M. Selina⁸⁴, I. Selyuzhenkov⁹⁷, S. Senyukov¹²⁹, J. J. Seo⁹⁴, D. Serebryakov¹⁴¹, L. Serkin⁶⁵, L. Šerkšnytė⁹⁵, A. Sevcenco⁶³, T. J. Shaba⁶⁸, A. Shabetai¹⁰³, R. Shahoyan³², A. Shangaraev¹⁴¹, B. Sharma⁹¹, D. Sharma⁴⁷, H. Sharma⁵⁴, M. Sharma⁹¹, S. Sharma⁷⁶, S. Sharma⁹¹, U. Sharma⁹¹, A. Shatat¹³¹, O. Sheibani¹¹⁶, K. Shigaki⁹², M. Shimomura⁷⁷, J. Shin¹², S. Shirinkin¹⁴¹, Q. Shou³⁹, Y. Sibiriak¹⁴¹, S. Siddhanta⁵², T. Siemiarczuk⁷⁹, T. F. Silva¹¹⁰, D. Silvermyr⁷⁵, T. Simantathammakul¹⁰⁵, R. Simeonov³⁶, B. Singh⁹¹, B. Singh⁹⁵, K. Singh⁴⁸, R. Singh⁸⁰, R. Singh⁹¹, R. Singh⁹⁷, S. Singh¹⁵, V. K. Singh¹³⁵, V. Singhal¹³⁵, T. Sinha⁹⁹, B. Sitar¹³, M. Sitta^{133,56}, T. B. Skaali¹⁹, G. Skorodumovs⁹⁴, N. Smirnov¹³⁸, R. J. M. Snellings⁵⁹, E. H. Solheim¹⁹, J. Song¹⁶, C. Sonnabend^{32,97}, J. M. Sonneveld⁸⁴, F. Soramel²⁷, A. B. Soto-Hernandez⁸⁸, R. Spijkers⁸⁴, I. Sputowska¹⁰⁷, J. Staa⁷⁵, J. Stachel⁹⁴, I. Stan⁶³, P. J. Steffanic¹²², T. Stellhorn¹²⁶, S. F. Stiefelmaier⁹⁴, D. Stocco¹⁰³, I. Storehaug¹⁹, N. J. Strangmann⁶⁴, P. Stratmann¹²⁶, S. Strazzi²⁵, A. Sturmiolo^{30,53}, C. P. Stylianidis⁸⁴, A. A. P. Suaide¹¹⁰, C. Suire¹³¹, M. Sukhanov¹⁴¹, M. Suljic³², R. Sultanov¹⁴¹, V. Sumberia⁹¹, S. Sumowidagdo⁸², M. Szymkowski¹³⁶, S. F. Taghavi⁹⁵, G. Taillepied⁹⁷, J. Takahashi¹¹¹, G. J. Tambave⁸⁰, S. Tang⁶, Z. Tang¹²⁰, J. D. Tapia Takaki¹¹⁸, N. Tapus¹¹³, L. A. Tarasovicova³⁷, M. G. Tartzila⁴⁵, G. F. Tassielli³¹, A. Tauro³², A. Tavira García¹³¹, G. Tejada Muñoz⁴⁴, L. Terlizzi²⁴, C. Terrevoli⁵⁰, S. Thakur⁴, D. Thomas¹⁰⁸, A. Tikhonov¹⁴¹, N. Tiltmann^{32,126}, A. R. Timmins¹¹⁶, M. Tkacik¹⁰⁶, T. Tkacik¹⁰⁶, A. Toia⁶⁴, R. Tokumoto⁹², S. Tomassini²⁵, K. Tomohiro⁹², N. Topilskaya¹⁴¹, M. Toppi⁴⁹, V. V. Torres¹⁰³, A. G. Torres Ramos³¹, A. Trifiró^{30,53}, T. Triloki⁹⁶, A. S. Triolo^{32,30,53}, S. Tripathy³², T. Tripathy⁴⁷, S. Trogolo²⁴, V. Trubnikov³, W. H. Trzaska¹¹⁷, T. P. Trzcinski¹³⁶, C. Tsolanta¹⁹, R. Tu³⁹, A. Tumkin¹⁴¹, R. Turrisi⁵⁴, T. S. Tveter¹⁹, K. Ullaland²⁰, B. Ulukutlu⁹⁵, S. Upadhyaya¹⁰⁷, A. Uras¹²⁸, M. Urioni¹³⁴, G. L. Usai²², M. Vala³⁷, N. Valle⁵⁵, L. V. R. van Doremalen⁵⁹, M. van Leeuwen⁸⁴, C. A. van Veen⁹⁴, R. J. G. van Weelden⁸⁴, P. Vande Vyvre³², D. Varga⁴⁶, Z. Varga⁴⁶, P. Vargas Torres⁶⁵, M. Vasileiou⁷⁸, A. Vasiliev^{141,e}, O. Vázquez Doce⁴⁹, O. Vazquez Rueda¹¹⁶, V. Vechernin¹⁴¹, E. Vercellin²⁴, S. Vergara Limón⁴⁴, R. Verma⁴⁷, L. Vermunt⁹⁷, R. Vértesi⁴⁶, M. Verweij⁵⁹, L. Vickovic³³, Z. Vilakazi¹²³, O. Villalobos Baillie¹⁰⁰, A. Villani²³, A. Vinogradov¹⁴¹, T. Virgili²⁸, M. M. O. Virta¹¹⁷, A. Vodopyanov¹⁴², B. Volkel³², M. A. Völkl⁹⁴, S. A. Voloshin¹³⁷, G. Volpe³¹, B. von Haller³², I. Vorobyev³², N. Vozniuk¹⁴¹, J. Vrláková³⁷, J. Wan³⁹, C. Wang³⁹, D. Wang³⁹, Y. Wang³⁹, Y. Wang⁶, Z. Wang³⁹, A. Wegrzynek³², F. T. Weiglhofer³⁸, S. C. Wenzel³², J. P. Wessels¹²⁶, J. Wiechula⁶⁴, J. Wikne¹⁹, G. Wilk⁷⁹, J. Wilkinson⁹⁷, G. A. Willems¹²⁶, B. Windelband⁹⁴, M. Winn¹³⁰, J. R. Wright¹⁰⁸, W. Wu³⁹, Y. Wu¹²⁰, Z. Xiong¹²⁰, R. Xu⁶, A. Yadav⁴², A. K. Yadav¹³⁵, Y. Yamaguchi⁹², S. Yang²⁰, S. Yano⁹², E. R. Yeats¹⁸, Z. Yin⁶, I.-K. Yoo¹⁶, J. H. Yoon⁵⁸, H. Yu¹², S. Yuan²⁰, A. Yuncu⁹⁴, V. Zaccolo²³, C. Zampolli³², F. Zanone⁹⁴, N. Zardoshti³², A. Zarochentsev¹⁴¹, P. Závada⁶², N. Zaviyalov¹⁴¹, M. Zhalov¹⁴¹, B. Zhang^{94,6}, C. Zhang¹³⁰, L. Zhang³⁹, M. Zhang^{127,6}, M. Zhang⁶, S. Zhang³⁹, X. Zhang⁶, Y. Zhang¹²⁰, Z. Zhang⁶, M. Zhao¹⁰, V. Zherebchevskii¹⁴¹, Y. Zhi¹⁰, D. Zhou⁶, Y. Zhou⁸³, J. Zhu^{54,6}, S. Zhu¹²⁰, Y. Zhu⁶, S. C. Zugravel⁵⁶, and N. Zurlo^{134,55}

(ALICE Collaboration)

¹*A.I. Alikhanyan National Science Laboratory (Yerevan Physics Institute) Foundation, Yerevan, Armenia*²*AGH University of Krakow, Cracow, Poland*³*Bogolyubov Institute for Theoretical Physics, National Academy of Sciences of Ukraine, Kiev, Ukraine*⁴*Bose Institute, Department of Physics and Centre for Astroparticle Physics and Space Science (CAPSS), Kolkata, India*⁵*California Polytechnic State University, San Luis Obispo, California, United States*

- ⁶*Central China Normal University, Wuhan, China*
- ⁷*Centro de Aplicaciones Tecnológicas y Desarrollo Nuclear (CEADEN), Havana, Cuba*
- ⁸*Centro de Investigación y de Estudios Avanzados (CINVESTAV), Mexico City and Mérida, Mexico*
- ⁹*Chicago State University, Chicago, Illinois, United States*
- ¹⁰*China Institute of Atomic Energy, Beijing, China*
- ¹¹*China University of Geosciences, Wuhan, China*
- ¹²*Chungbuk National University, Cheongju, Republic of Korea*
- ¹³*Comenius University Bratislava, Faculty of Mathematics, Physics and Informatics, Bratislava, Slovak Republic*
- ¹⁴*Creighton University, Omaha, Nebraska, United States*
- ¹⁵*Department of Physics, Aligarh Muslim University, Aligarh, India*
- ¹⁶*Department of Physics, Pusan National University, Pusan, Republic of Korea*
- ¹⁷*Department of Physics, Sejong University, Seoul, Republic of Korea*
- ¹⁸*Department of Physics, University of California, Berkeley, California, United States*
- ¹⁹*Department of Physics, University of Oslo, Oslo, Norway*
- ²⁰*Department of Physics and Technology, University of Bergen, Bergen, Norway*
- ²¹*Dipartimento di Fisica, Università di Pavia, Pavia, Italy*
- ²²*Dipartimento di Fisica dell'Università and Sezione INFN, Cagliari, Italy*
- ²³*Dipartimento di Fisica dell'Università and Sezione INFN, Trieste, Italy*
- ²⁴*Dipartimento di Fisica dell'Università and Sezione INFN, Turin, Italy*
- ²⁵*Dipartimento di Fisica e Astronomia dell'Università and Sezione INFN, Bologna, Italy*
- ²⁶*Dipartimento di Fisica e Astronomia dell'Università and Sezione INFN, Catania, Italy*
- ²⁷*Dipartimento di Fisica e Astronomia dell'Università and Sezione INFN, Padova, Italy*
- ²⁸*Dipartimento di Fisica 'E.R. Caianiello' dell'Università and Gruppo Collegato INFN, Salerno, Italy*
- ²⁹*Dipartimento DISAT del Politecnico and Sezione INFN, Turin, Italy*
- ³⁰*Dipartimento di Scienze MIFT, Università di Messina, Messina, Italy*
- ³¹*Dipartimento Interateneo di Fisica 'M. Merlin' and Sezione INFN, Bari, Italy*
- ³²*European Organization for Nuclear Research (CERN), Geneva, Switzerland*
- ³³*Faculty of Electrical Engineering, Mechanical Engineering and Naval Architecture, University of Split, Split, Croatia*
- ³⁴*Faculty of Engineering and Science, Western Norway University of Applied Sciences, Bergen, Norway*
- ³⁵*Faculty of Nuclear Sciences and Physical Engineering, Czech Technical University in Prague, Prague, Czech Republic*
- ³⁶*Faculty of Physics, Sofia University, Sofia, Bulgaria*
- ³⁷*Faculty of Science, P.J. Šafárik University, Košice, Slovak Republic*
- ³⁸*Frankfurt Institute for Advanced Studies, Johann Wolfgang Goethe-Universität Frankfurt, Frankfurt, Germany*
- ³⁹*Fudan University, Shanghai, China*
- ⁴⁰*Gangneung-Wonju National University, Gangneung, Republic of Korea*
- ⁴¹*Gauhati University, Department of Physics, Guwahati, India*
- ⁴²*Helmholtz-Institut für Strahlen- und Kernphysik, Rheinische Friedrich-Wilhelms-Universität Bonn, Bonn, Germany*
- ⁴³*Helsinki Institute of Physics (HIP), Helsinki, Finland*
- ⁴⁴*High Energy Physics Group, Universidad Autónoma de Puebla, Puebla, Mexico*
- ⁴⁵*Horia Hulubei National Institute of Physics and Nuclear Engineering, Bucharest, Romania*
- ⁴⁶*HUN-REN Wigner Research Centre for Physics, Budapest, Hungary*
- ⁴⁷*Indian Institute of Technology Bombay (IIT), Mumbai, India*
- ⁴⁸*Indian Institute of Technology Indore, Indore, India*
- ⁴⁹*INFN, Laboratori Nazionali di Frascati, Frascati, Italy*
- ⁵⁰*INFN, Sezione di Bari, Bari, Italy*
- ⁵¹*INFN, Sezione di Bologna, Bologna, Italy*
- ⁵²*INFN, Sezione di Cagliari, Cagliari, Italy*
- ⁵³*INFN, Sezione di Catania, Catania, Italy*
- ⁵⁴*INFN, Sezione di Padova, Padova, Italy*
- ⁵⁵*INFN, Sezione di Pavia, Pavia, Italy*
- ⁵⁶*INFN, Sezione di Torino, Turin, Italy*
- ⁵⁷*INFN, Sezione di Trieste, Trieste, Italy*
- ⁵⁸*Inha University, Incheon, Republic of Korea*
- ⁵⁹*Institute for Gravitational and Subatomic Physics (GRASP), Utrecht University/Nikhef, Utrecht, Netherlands*
- ⁶⁰*Institute of Experimental Physics, Slovak Academy of Sciences, Košice, Slovak Republic*
- ⁶¹*Institute of Physics, Homi Bhabha National Institute, Bhubaneswar, India*
- ⁶²*Institute of Physics of the Czech Academy of Sciences, Prague, Czech Republic*
- ⁶³*Institute of Space Science (ISS), Bucharest, Romania*
- ⁶⁴*Institut für Kernphysik, Johann Wolfgang Goethe-Universität Frankfurt, Frankfurt, Germany*

- ⁶⁵*Instituto de Ciencias Nucleares, Universidad Nacional Autónoma de México, Mexico City, Mexico*
- ⁶⁶*Instituto de Física, Universidade Federal do Rio Grande do Sul (UFRGS), Porto Alegre, Brazil*
- ⁶⁷*Instituto de Física, Universidad Nacional Autónoma de México, Mexico City, Mexico*
- ⁶⁸*iThemba LABS, National Research Foundation, Somerset West, South Africa*
- ⁶⁹*Jeonbuk National University, Jeonju, Republic of Korea*
- ⁷⁰*Johann-Wolfgang-Goethe Universität Frankfurt Institut für Informatik, Fachbereich Informatik und Mathematik, Frankfurt, Germany*
- ⁷¹*Korea Institute of Science and Technology Information, Daejeon, Republic of Korea*
- ⁷²*KTO Karatay University, Konya, Turkey*
- ⁷³*Laboratoire de Physique Subatomique et de Cosmologie, Université Grenoble-Alpes, CNRS-IN2P3, Grenoble, France*
- ⁷⁴*Lawrence Berkeley National Laboratory, Berkeley, California, United States*
- ⁷⁵*Lund University Department of Physics, Division of Particle Physics, Lund, Sweden*
- ⁷⁶*Nagasaki Institute of Applied Science, Nagasaki, Japan*
- ⁷⁷*Nara Women's University (NWU), Nara, Japan*
- ⁷⁸*National and Kapodistrian University of Athens, School of Science, Department of Physics, Athens, Greece*
- ⁷⁹*National Centre for Nuclear Research, Warsaw, Poland*
- ⁸⁰*National Institute of Science Education and Research, Homi Bhabha National Institute, Jatni, India*
- ⁸¹*National Nuclear Research Center, Baku, Azerbaijan*
- ⁸²*National Research and Innovation Agency - BRIN, Jakarta, Indonesia*
- ⁸³*Niels Bohr Institute, University of Copenhagen, Copenhagen, Denmark*
- ⁸⁴*Nikhef, National institute for subatomic physics, Amsterdam, Netherlands*
- ⁸⁵*Nuclear Physics Group, STFC Daresbury Laboratory, Daresbury, United Kingdom*
- ⁸⁶*Nuclear Physics Institute of the Czech Academy of Sciences, Husinec-Řež, Czech Republic*
- ⁸⁷*Oak Ridge National Laboratory, Oak Ridge, Tennessee, United States*
- ⁸⁸*Ohio State University, Columbus, Ohio, United States*
- ⁸⁹*Physics department, Faculty of science, University of Zagreb, Zagreb, Croatia*
- ⁹⁰*Physics Department, Panjab University, Chandigarh, India*
- ⁹¹*Physics Department, University of Jammu, Jammu, India*
- ⁹²*Physics Program and International Institute for Sustainability with Knotted Chiral Meta Matter (SKCM2), Hiroshima University, Hiroshima, Japan*
- ⁹³*Physikalisches Institut, Eberhard-Karls-Universität Tübingen, Tübingen, Germany*
- ⁹⁴*Physikalisches Institut, Ruprecht-Karls-Universität Heidelberg, Heidelberg, Germany*
- ⁹⁵*Physik Department, Technische Universität München, Munich, Germany*
- ⁹⁶*Politecnico di Bari and Sezione INFN, Bari, Italy*
- ⁹⁷*Research Division and ExtreMe Matter Institute EMMI, GSI Helmholtzzentrum für Schwerionenforschung GmbH, Darmstadt, Germany*
- ⁹⁸*Saga University, Saga, Japan*
- ⁹⁹*Saha Institute of Nuclear Physics, Homi Bhabha National Institute, Kolkata, India*
- ¹⁰⁰*School of Physics and Astronomy, University of Birmingham, Birmingham, United Kingdom*
- ¹⁰¹*Sección Física, Departamento de Ciencias, Pontificia Universidad Católica del Perú, Lima, Peru*
- ¹⁰²*Stefan Meyer Institut für Subatomare Physik (SMI), Vienna, Austria*
- ¹⁰³*SUBATECH, IMT Atlantique, Nantes Université, CNRS-IN2P3, Nantes, France*
- ¹⁰⁴*Sungkyunkwan University, Suwon City, Republic of Korea*
- ¹⁰⁵*Suranaree University of Technology, Nakhon Ratchasima, Thailand*
- ¹⁰⁶*Technical University of Košice, Košice, Slovak Republic*
- ¹⁰⁷*The Henryk Niewodniczanski Institute of Nuclear Physics, Polish Academy of Sciences, Cracow, Poland*
- ¹⁰⁸*The University of Texas at Austin, Austin, Texas, United States*
- ¹⁰⁹*Universidad Autónoma de Sinaloa, Culiacán, Mexico*
- ¹¹⁰*Universidade de São Paulo (USP), São Paulo, Brazil*
- ¹¹¹*Universidade Estadual de Campinas (UNICAMP), Campinas, Brazil*
- ¹¹²*Universidade Federal do ABC, Santo Andre, Brazil*
- ¹¹³*Universitatea Nationala de Stiinta si Tehnologie Politehnica Bucuresti, Bucharest, Romania*
- ¹¹⁴*University of Cape Town, Cape Town, South Africa*
- ¹¹⁵*University of Derby, Derby, United Kingdom*
- ¹¹⁶*University of Houston, Houston, Texas, United States*
- ¹¹⁷*University of Jyväskylä, Jyväskylä, Finland*
- ¹¹⁸*University of Kansas, Lawrence, Kansas, United States*
- ¹¹⁹*University of Liverpool, Liverpool, United Kingdom*
- ¹²⁰*University of Science and Technology of China, Hefei, China*
- ¹²¹*University of South-Eastern Norway, Kongsberg, Norway*
- ¹²²*University of Tennessee, Knoxville, Tennessee, United States*

- ¹²³*University of the Witwatersrand, Johannesburg, South Africa*
¹²⁴*University of Tokyo, Tokyo, Japan*
¹²⁵*University of Tsukuba, Tsukuba, Japan*
¹²⁶*Universität Münster, Institut für Kernphysik, Münster, Germany*
¹²⁷*Université Clermont Auvergne, CNRS/IN2P3, LPC, Clermont-Ferrand, France*
¹²⁸*Université de Lyon, CNRS/IN2P3, Institut de Physique des 2 Infinis de Lyon, Lyon, France*
¹²⁹*Université de Strasbourg, CNRS, IPHC UMR 7178, F-67000 Strasbourg, France, Strasbourg, France*
¹³⁰*Université Paris-Saclay, Centre d'Etudes de Saclay (CEA), IRFU, Département de Physique Nucléaire (DPhN), Saclay, France*
¹³¹*Université Paris-Saclay, CNRS/IN2P3, IJCLab, Orsay, France*
¹³²*Università degli Studi di Foggia, Foggia, Italy*
¹³³*Università del Piemonte Orientale, Vercelli, Italy*
¹³⁴*Università di Brescia, Brescia, Italy*
¹³⁵*Variable Energy Cyclotron Centre, Homi Bhabha National Institute, Kolkata, India*
¹³⁶*Warsaw University of Technology, Warsaw, Poland*
¹³⁷*Wayne State University, Detroit, Michigan, United States*
¹³⁸*Yale University, New Haven, Connecticut, United States*
¹³⁹*Yonsei University, Seoul, Republic of Korea*
¹⁴⁰*Zentrum für Technologie und Transfer (ZTT), Worms, Germany*
¹⁴¹*Affiliated with an institute covered by a cooperation agreement with CERN*
¹⁴²*Affiliated with an international laboratory covered by a cooperation agreement with CERN*

^aAlso at: Max-Planck-Institut für Physik, Munich, Germany.

^bAlso at: Italian National Agency for New Technologies, Energy and Sustainable Economic Development (ENEA), Bologna, Italy.

^cAlso at: Dipartimento DET del Politecnico di Torino, Turin, Italy.

^dAlso at: Yildiz Technical University, Istanbul, Türkiye.

^eDeceased.

^fAlso at: An institution covered by a cooperation agreement with CERN.

^gAlso at: Department of Applied Physics, Aligarh Muslim University, Aligarh, India.

^hAlso at: Institute of Theoretical Physics, University of Wrocław, Poland.